

**AUTOMATED COOL-FLAME RECOGNITION IN RAINBOW  
SCHLIEREN IMAGES OF DIESEL COMBUSTION**

A Thesis

Presented to

the Faculty of the Honors College

University of Alabama in Huntsville

In Fulfillment

of the Requirements of HON 499: Honors Capstone

By

Noah Milivojevic

December 2025

## ***Abstract***

Despite the many improvements in diesel combustion since the first diesel engines 130 years ago, they still represent the most efficient road-transportation powertrain available and still have possible efficiency gains. A major area of interest in the field is cool-flame combustion and ignition evolution; however, these phenomena are short-lived (sub millisecond scale) and occur at extreme conditions, making them hard to study. Studying reacting fuel sprays in specialized test facilities, with kilohertz speed imaging allows for time- and space-resolved data of individual combustion events. Rainbow Schlieren Deflectometry imaging is used to obtain spatially resolved density measurements of a fuel spray as it is injected, mixed, and combusted in a constant pressure chamber at temperatures and pressures representative of diesel engine operation. A common technique in analysis is to average a statistically significant number of injections to achieve an “average” injection that is easier to study; however, this technique results in different regimes (mixed air/fuel, cool flame, and hot flame) with fundamentally different chemical and thermodynamic properties to be overlaid. An algorithm is developed to distinguish the unburnt fuel, cool flame combustion, and hot flame combustion regions, thus allowing each mixing and combustion regime to be studied separately. The introduction of statistical and machine learning techniques allows for confidence intervals to be placed on each region.

## ***Acknowledgements***

I would like to thank Dr. Joshua Bittle and Dr. Allen Parker for their mentorship in developing the code presented here and providing the sample data used to test this code, as well as the National Science Foundation's Research Experiences for Undergraduates program for the opportunity to work on this project. I would additionally like to thank Gaurav Bharatha for general support when developing this code. I would like to thank Dr. Keith Hollingsworth for his help in preparing this manuscript and his mentorship throughout my undergraduate degree. Finally, I would like to thank Ann Lorey for instilling her love of science in all of her students, myself included. May she rest in peace.

# Table of Contents

<b>ABSTRACT.....</b>	ii
<b>ACKNOWLEDGEMENTS.....</b>	iii
<b>TABLE OF CONTENTS.....</b>	iv
<b>LIST OF FIGURES.....</b>	v
<b>LIST OF TABLES.....</b>	ix
<b>NOMENCLATURE.....</b>	x
<b>CHAPTER 1. INTRODUCTION.....</b>	1
1.1 Wider applications of diesel combustion research.....	1
1.2 Introduction to diesel engines.....	2
1.3 Introduction to cool flames.....	3
1.4 Constant Pressure Flow Rig.....	3
1.5 Introduction to Rainbow Schlieren Deflectometry.....	5
1.6 Rainbow filter design and selection.....	6
1.7 Quantitative Rainbow Schlieren Deflectometry.....	10
1.8 Limitations of RSD.....	15
<b>CHAPTER 2. LITERATURE REVIEW.....</b>	18
2.1 Representative Phenomena of Cyclic Turbulent Combustion in High-Pressure Fuel Sprays.....	22
2.2 Quantitative concentration measurements in a turbulent helium jet using rainbow schlieren deflectometry.....	23
2.3 Phase boundary detection in transient, evaporating high-pressure fuel sprays by rainbow schlieren deflectometry.....	24
<b>CHAPTER 3. FLOW REGIME CLASSIFICATION ALGORITHM.....</b>	25
3.1 Introduction.....	25
3.2 Experimental Setup.....	25
3.3 Code Requirements.....	26
3.4 Calibration.....	27
3.5 Software Filters Used.....	28
3.5.1 Uniform Filter.....	29
3.5.2 Low-, High-, and Band-pass filters.....	29
3.5.3 Erosion.....	31
3.11 Discussion.....	54
<b>CHAPTER 4. RECAPITULATION AND CONCLUSIONS.....</b>	55
<b>REFERENCES.....</b>	56
<b>APPENDIX A.....</b>	60

## ***List of Figures***

<b>Figure 1.1</b>	A pressure-volume diagram of the diesel cycle, the thermodynamic operating principle of a diesel engine [8].	3
<b>Figure 1.2</b>	Diagrams of the experimental setup and instrumentation.	4
<b>Figure 1.3</b>	A diagram describing the Rainbow Schlieren Deflectometry setup [15].	5
<b>Figure 1.4</b>	An example of a radial filter, with several representative points indicated.	7
<b>Figure 1.5</b>	Comparison of radial and linear filter sensitivity. In both cases point B corresponds to zero deflection.	8
<b>Figure 1.6</b>	Sample false color RSD image showing fuel spray shape and coordinate system. Blue indicates a positive density gradient (left side of a dense spray), while red indicates a negative density gradient (right side of a dense spray).	9
<b>Figure 1.7</b>	Decomposition of the Phillips circle pattern into its individual red, green, and blue channels, shown in greyscale.	10
<b>Figure 1.8</b>	Decomposition of the Phillips circle pattern into its individual hue (shown in true hue), saturation, and value channels (shown in grayscale).	11
<b>Figure 1.9</b>	A visual representation of HSV space, with a cross section view [18].	13
<b>Figure 1.10</b>	A variety of injections, all at 1.9 ms after injection. Blue-green indicates RSD data, yellow indicates hydroxyl chemical activity, and magenta indicates soot formation.	16
<b>Figure 3.1</b>	Effect of applying the uniform filter and gaussian filter to the Phillips circle pattern. Note that although the general blurring effect is the same for both filters, the uniform filter better preserves some small scale features such as the background grid.	29
<b>Figure 3.2</b>	An example of various Gaussian filters applied in low-, high-, and band-pass modes to the Phillips circle pattern.	30
<b>Figure 3.3</b>	Examples of image erosion on both greyscale and binarized versions of the Phillips test pattern.	31

<b>Figure 3.4</b>	Examples of image dilation on both greyscale and binarized versions of the Phillips test pattern.	32
<b>Figure 3.5</b>	An example of area opening using the RCA "Indian Head" Test Pattern. Note that regions with many small details are merged into larger blocks with roughly the same shape and size as the original.	33
<b>Figure 3.6</b>	An example of area closing using the RCA "Indian Head" Test Pattern. Note that small features are removed (such as text and the small horizontal bars at the bottom), while larger features are preserved (such as the large horizontal bars).	34
<b>Figure 3.7</b>	An example of the white top hat filter using the RCA "Indian Head" Test Pattern. Note that the filter extracts only small details (such as the test lines), while rejecting larger structures such as the large rings and grid.	35
<b>Figure 3.8</b>	Anatomy of a multimodal distribution. Many multimodal distributions can be broken up into multiple unimodal distributions, especially those multimodal distributions which result from the measurement of multiple phenomena happening simultaneously.	36
<b>Figure 3.9</b>	Comparison of true color (left) and isolated saturation (right, yellow/blue scale) RSD images at 3.5 ms after injection for an n-heptane spray at ambient conditions of 800 K and 30 bar.	37
<b>Figure 3.10</b>	Comparison of histogram plots of the injection saturation image shown in Figure 3.9 (blue) and an image with no spray visible (orange). The green dashed line shows the mean of the background saturation distribution, while the red dashed line represents a threshold cutoff value located two standard deviations from the mean of the background saturation distribution. The x-axis shows saturation value, while the y-axis shows the count of pixels exhibiting the given saturation value. Axis units are arbitrary.	38
<b>Figure 3.11</b>	RSD image of isolated spray/hot flame at 3.5 ms after injection, 800 K and 30 bar ambient conditions.	39

<b>Figure 3.12</b>	A chronological series of RSD images of an n-heptane at 800 K, 30 bar ambient conditions. The lower part of the fluid spray (circled in the middle frame) seems to "disappear" and then "reappear" as a hot flame at $t=2.70$ ms. This intermediate step, where the refractive index of the circled regions happens to match the background refractive index, is the cool flame region, as it appears chronologically between the non-reacting and hot flame flow regimes.	40
<b>Figure 3.13</b>	Detail of Figure 3.12 at $t=1.95$ ms, highlighting the similarities and differences in the background and cool flame regions.	41
<b>Figure 3.14</b>	Comparison of true color (left) and isolated value (right, yellow/blue scale) RSD images at 3.5 ms after injection for an n-heptane spray at ambient conditions of 800 K and 30 bar.	42
<b>Figure 3.15</b>	Results of applying a difference of gaussians filter (left) to the value channel image obtained in Figure 3.14, followed by applying a uniform filter to produce a value edge count intensity (right).	43
<b>Figure 3.16</b>	Histogram plot comparison of background edge count value intensities (orange) and spray edge count value intensities (blue, $t=3.5$ ms). The x-axis is proportional to the number of edges within a given region, while the y-axis represents the count of pixels that have that number of neighboring edges. The units of both axes are arbitrary. Note that the range of edge counts corresponding to the background (left half of the graph) does not follow any simple Gaussian patterns. The right half of the graph, corresponding to edge densities only found in frames with an injection, has a shape that may be a mixture of gaussians. The red line is a smoothing of this region that is used to estimate the number of peaks needed for the mixture of Gaussians method.	44
<b>Figure 3.17</b>	RSD image of isolated cool flame at 3.5 ms after injection, 800 K and 30 bar ambient conditions.	46
<b>Figure 3.18</b>	Comparison of input RSD image (left) and cool flame and spray/hot flame contours found by the detection filters (right). Spray and hot flame are shown in red, while cool flame is shown in yellow. Image taken at 0 ms after start of injection.	50

<b>Figure 3.19</b>	Comparison of input RSD image (left) and cool flame and spray/hot flame contours found by the detection filters (right). Spray and hot flame are shown in red, while cool flame is shown in yellow. Image taken at 0.45 ms after start of injection.	51
<b>Figure 3.20</b>	Comparison of input RSD image (left) and cool flame and spray/hot flame contours found by the detection filters (right). Spray and hot flame are shown in red, while cool flame is shown in yellow. Image taken at 1.95 ms after the start of injection.	52
<b>Figure 3.21</b>	Comparison of input RSD image (left) and cool flame and spray/hot flame contours found by the detection filters (right). Spray and hot flame are shown in red, while cool flame is shown in yellow. Image taken at 3.2 ms after start of injection.	53
<b>Figure 3.22</b>	Comparison of input RSD image (left) and cool flame and spray/hot flame contours found by the detection filters (right). Spray and hot flame are shown in red, while cool flame is shown in yellow. Image taken at 6.2 ms after start of injection.	54

## ***List of Tables***

**Table 2.1**      List of articles relevant to this work

19

## ***Nomenclature***

B	Blue
CPFR	Constant Pressure Flow Rig
DNS	Direct Numerical Simulation
ECN	Engines and Combustion Network
G	Green
H	Hue
HSI	Hue, Saturation, Intensity coordinates
HSV	Hue, Saturation, Value coordinates
PDF	Probability Distribution Function
R	Red
RGB	Red, Green, Blue coordinates
RSD	Rainbow Schlieren Deflectometry
S	Saturation
UA ECL	University of Alabama Engines and Combustion Lab
V	Value

## CHAPTER 1. INTRODUCTION

This study aims to develop a method of automatically categorizing background, fuel spray, cold flame, and hot flame regions in a high-speed Rainbow Schlieren Deflectometry (RSD) image of a combusting diesel injection. The impetus to this project was the processing of RSD data from studies conducted at the University of Alabama Engines and Combustion Lab (UA ECL), however, the system developed here is intended to be applicable to a wide range of combustion-RSD setups through the use of statistical and machine-learning methods.

### 1.1 Wider applications of diesel combustion research

The wider application of the diesel combustion work is in the verification of numerical models of combustion. By studying simplified combustion cases with a reduced number of confounding variables (no spray impingement, quiescent background flow, etc), the basic fluid dynamics and chemical kinetics of numerical models can be tested against real-world data [1]. Modern diesel engines can reach pre-combustion temperatures of up to 1000 K and pressures of up to 100 bar [2], often reaching supercritical fluid conditions and leaving the ideal gas regime [3]. A common standard injection setup is 900 K at 60 bar as specified by the Engines and Combustion Network (ECN) Spray A standard [4]. As such, there is little data that can be used to verify computer models of combustion.

Macroscopic properties, such as engine power and emissions composition, are relatively easy to access and compare with theoretical values due to the fact that they are located outside of the engine. The actual fuel injection, mixing, and combustion process is harder to investigate, as it occurs at temperatures, pressures, and time scales that are less forgiving to measurement equipment. The availability of both measured data, as well as the validation of the accuracy of

computational models of combustion in these extreme conditions allows the for advances in the design of diesel injectors, alternative fuels, and diesel engine operation that can be used to improve engine performance and engine efficiency, as well as reduce engine emissions [5].

## **1.2 Introduction to diesel engines**

Four-stroke diesel engines remain an attractive form of power production for heavy applications due to their high power density, durability, and fuel flexibility [6]. Four-stroke diesel engines generate power through the combustion of diesel fuel in a piston assembly. Atmospheric air is compressed in the piston during the compression stroke, diesel fuel is injected into the highly compressed air, and the diesel fuel autoignites due to the high temperatures and pressures developed by the compression stroke [7]. Combustion further increases the temperature of the gas in the cylinder. Expansion of the cylinder volume produces useful work, and the combustion products are exhausted. Figure 1.1 shows the Diesel cycle on a pressure-volume diagram [8]; the combustion process is represented by the line 2-3 on the diagram. While combustion is an ideally isobaric process, real engine behaviour rarely reflects this [8].

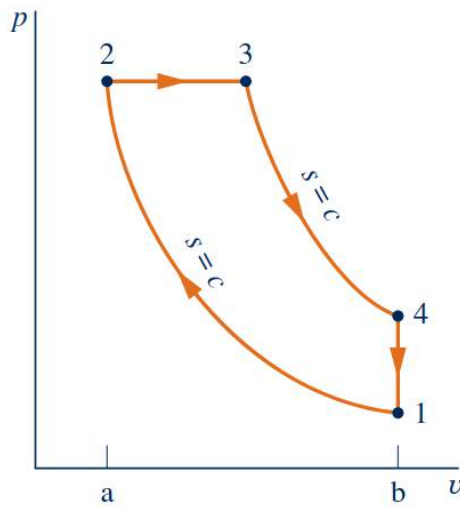


**Figure 1.1** A pressure-volume diagram of the diesel cycle, the thermodynamic operating principle of a diesel engine [8].

### 1.3 Introduction to cool flames

Diesel combustion happens in four main phases: mixing, cool flame combustion, hot flame combustion, and extinction [9, 10]. Cool flame combustion is generally understood to be a precursor to the hot-flame combustion, thus, understanding cool flame combustion better will help to improve the combustion efficiency of diesel engines, leading to higher power and lowered emissions [11]. Additionally, cool-flame chemistry produces products that differ from that of typical hot-flame chemistry; therefore, controlling cool-flame behaviour allows a designer greater control over tailpipe emissions composition. The cool-flame phenomenon was experimentally identified in previous diesel combustion research performed by Allen Parker and Joshua Bittle at the UA ECL, though the full implications of the cool flame were not considered in their studies [12].

### 1.4 Constant Pressure Flow Rig

The main impetus for the creation of this cool flame detection code was to process data produced by the Constant Pressure Flow Rig (CPFR) at the UA ECL. A diagram of the CPFR can be seen in Figure 1.2.

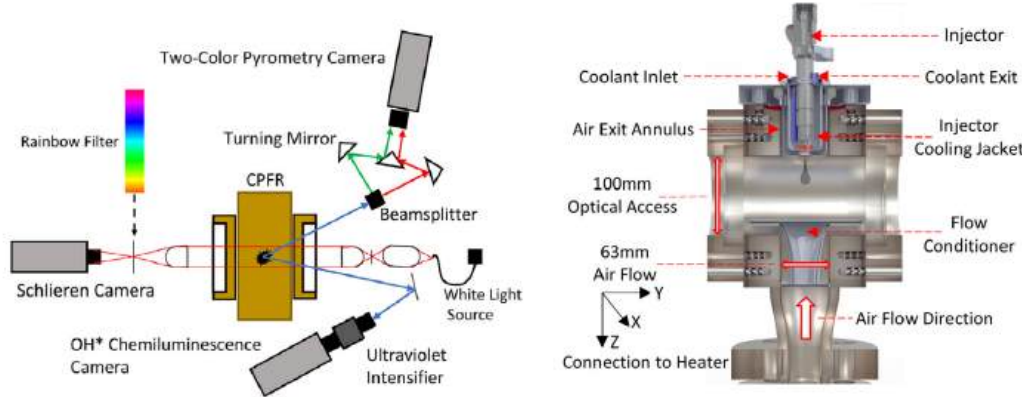


**Figure 1.2** Diagrams of the experimental setup and instrumentation.

Hot, high pressure air flows into the chamber, simulating cylinder conditions at the end of the compression stroke, when fuel is injected. A standard diesel engine injector (interchangeable) is used to inject a fuel charge into the chamber. The combustion products are then fed through exhaust vents. The chamber air inflow and exhaust are continuous (as opposed to the discrete intake and exhaust steps in a classical combustion engine) in order to prevent soot buildup on the chamber windows. This allows for the chamber to be run for arbitrarily large numbers of injections between cleanings, as opposed to optical engines that must be cleaned more often. Combustion happens at constant pressure due to the continuous air inflow/exhaust. Thermocouples and pressure transducers mounted inside the chamber monitor general chamber conditions. Optical ports allow for any combination of standard optical techniques to be used; most commonly, this is Rainbow Schlieren Deflectometry (RSD, measuring density distributions), two-color pyrometry (measuring soot distribution and temperature), and hydroxyl radical chemiluminescence (measuring the distribution of chemical reactions involving hydroxyl

radicals). This setup has been widely used in studies conducted by the ECL [3, 12, 14, 18, 24, 25, 26]. In this study only the RSD diagnostic is considered.

### 1.5 Introduction to Rainbow Schlieren Deflectometry

Rainbow Schlieren Deflectometry imaging is a technique that allows any conventional color camera to “see” the index of refraction within a working fluid. Through the use of digital cameras, this data can be quantized, allowing accurate measurement of refractive index that can be correlated to density gradients and used to derive other thermodynamic properties such as temperature, pressure, and mixture ratio [13, 16].

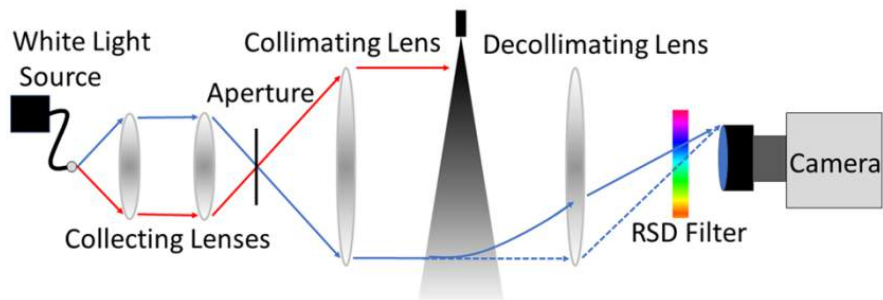


**Figure 1.3** A diagram describing the Rainbow Schlieren Deflectometry setup [14].

RSD is a system similar to regular Schlieren deflectometry. A basic schematic can be found in Figure 1.3. A bright white light source is run through a set of focusing lenses to focus the light to a point source. This is then run through a collimating lens, aligning the light rays to be parallel. The collimated light is then run through whatever fluid is being experimented on. Density gradients produce a change in the index of refraction, this, in turn, deflects the otherwise collimated light. The light then passes through a decollimating lens, focusing the collimated light back down to a point. However, light that has been deflected by the working fluid will enter the decollimating lens at a different angle and at a different point on the lens than undeflected light, meaning it will not be focused onto the same point as the collimated light [15].

By placing a transparent rainbow filter at the focus point of the decollimating lens, the light can be colored depending on how far the collimated light was deflected from its original path of travel by density gradients in the working fluid. A color camera placed after the color filter measures the hue of each pixel so that it can be correlated to a deflection distance on the filter. With knowledge of the optical setup, this deflection distance can be converted to an angle, which corresponds to the refractive index of the working fluid along a given ray of light. The refractive index corresponds to the density gradient at any given point; that is, given an uneven density distribution, a light ray will bend towards the region of higher density.

## 1.6 Rainbow filter design and selection

The bending of the light has both a magnitude (magnitude of the density gradient) and direction (direction of the density gradient). Rainbow filters can only measure the magnitude of deflection but they can be designed to only react to deflections in certain directions, thus, rainbow filter design and selection becomes application specific.

Radial rainbow filters that are sensitive to deflections in all directions exist and have been used [13, 15], but suffer from the limitations of hysteresis near the zero point. An ideal point source would mean that the zero-deflection point at the center of the filter would have zero width, requiring much finer positioning, as compared to a linear filter, which will always be equally sensitive no matter where the light is focused. Figure 1.4 shows an example of this, where points A, B, and C will all register as “zero” on the filter, despite the fact that they lie on different points on the filter. An additional issue is that point B will be much more sensitive to deflection, where a much smaller deflection to the left is needed to cause the light to pass through the colored portion of the filter than rightwards deflection. The result of this is that the

schlieren system will overreport deflections to the left and underreport deflections to the right; ideally, the filter should be equally sensitive to deflections in all directions.

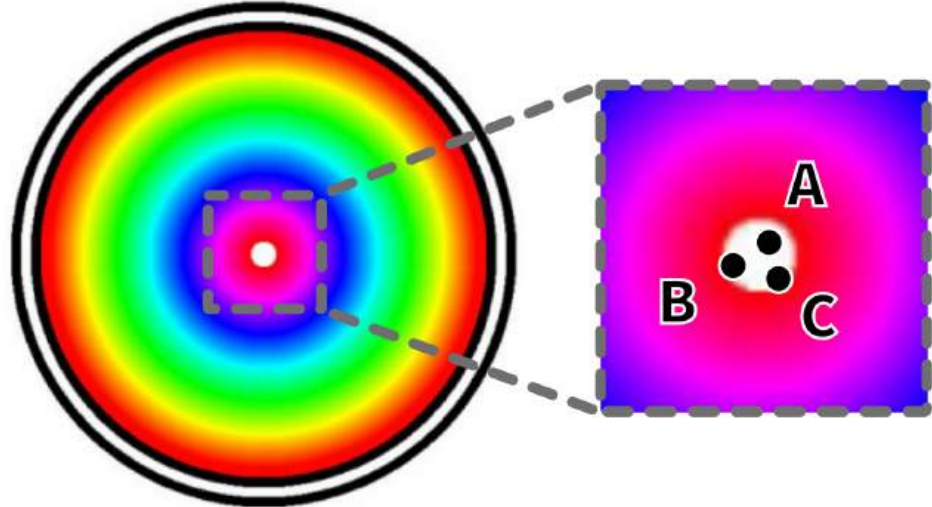


**Figure 1.4** An example of a radial filter, with several representative points indicated.

An additional limitation of the radial rainbow filter is that it cannot differentiate the direction of the deflection, whereas a linear filter can differentiate between positive and negative deflection. Points A, B, and C in Figure 1.5 all have the same relative position on the radial (left) and linear (right) filters, but result in different filter responses. On the radial filter, point B is distinguishable from A and C, but A and C are indistinguishable from each other. On the linear filter, C is distinguishable, but A and B are indistinguishable (hence why the A-B axis is considered “dead” and the B-C axis is considered “live”). The result is that radial filters measure the magnitude of deflection, but not the direction of deflection. Linear filters measure the deflection in one direction, and ignore deflections in the perpendicular direction. Essentially, radial filters will provide the gradient of the density distribution field, whereas linear filters will provide the partial derivative of the density distribution field in one of the Cartesian directions.

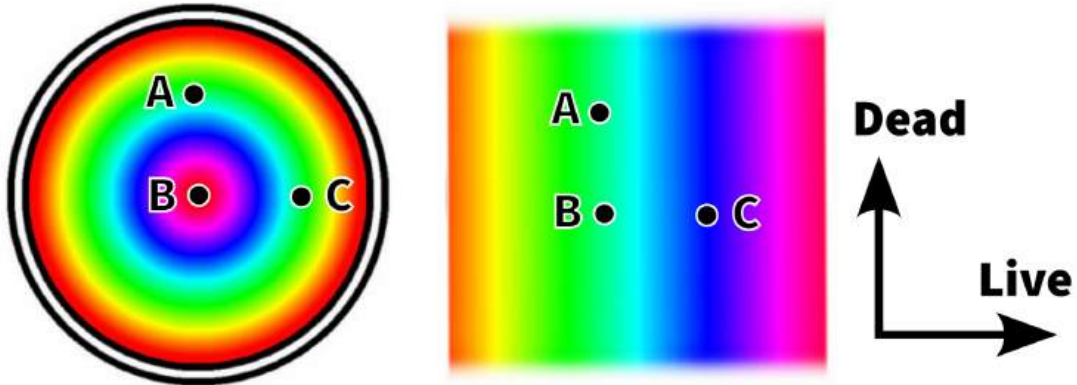


**Figure 1.5** Comparison of radial and linear filter sensitivity. In both cases point B corresponds to zero deflection.

In cases where the density distribution can be assumed to be relatively continuous and the direction of deflection is well predicted by the geometry of the problem, such as the spherical flames studied by Feikema, a radial filter is appropriate, as the assumption of the direction of the deflection vector can be combined with the measured deflection magnitude to reconstruct the entire deflection vector [13].

However, in this study, the turbulent nature of diesel injection and combustion means that assumptions cannot be made about the direction of the deflection vector. Additionally, small-scale flow structures that are smaller than the resolution of the camera mean that the deflection direction for any given pixel is essentially independent of the neighboring pixels. As such, a linear filter becomes more attractive, as a simple line integral along the “live” direction of the rainbow filter can be used to reconstruct the density field.

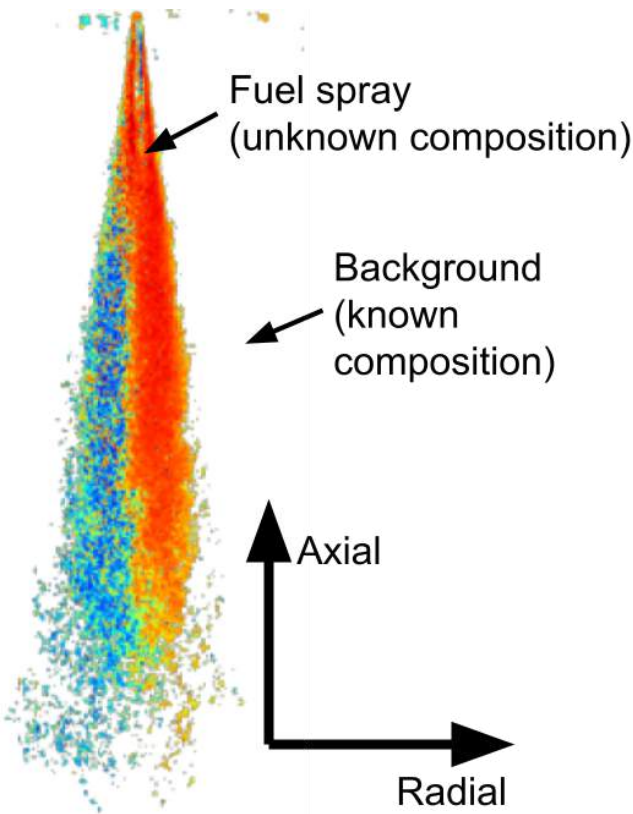


**Figure 1.6** Sample false color RSD image showing fuel spray shape and coordinate system. Blue indicates a positive density gradient (left side of a dense spray), while red indicates a negative density gradient (right side of a dense spray).

As seen in Figure 1.6, diesel injections can be assumed to be pseudo conical, that is, they should be relatively uniform in the axial direction, with most of the interesting gradients happening in the radial direction. Additionally, the extrema in the radial direction can be assumed to be at known values, in this case the background air composition. Aligning the “dead” axis of the linear filter with the axial direction and the “live” axis in the radial direction allows maximum use from the limitations of the linear filter, by using the “live” direction to measure the

direction of highest density gradient change while also allowing the known composition on either side of the fuel spray to “anchor” the integration of the density gradient differential.

## 1.7 Quantitative Rainbow Schlieren Deflectometry

Because an RSD system places a numerical value on the deflection, this allows an RSD system to be used for quantitative measurements of density, whereas most classical schlieren systems are limited to qualitative descriptions about the general flow structure [16]. As this thesis focuses on the classification of combustion regimes and does not directly utilize the quantitative aspects of RSD, the full mathematical treatment of converting hue to density gradient is not presented; however, the end goal is that this system can be implemented in tandem with quantitative RSD systems in order to improve the accuracy of results. A more rigorous mathematical overview may be found in a variety of existing quantitative RSD work [13, 14, 16, 17].

The basic premise underpinning the use of RSD for quantitative studies is the transformation of light information from the photosensor from Red-Green-Blue (RGB) coordinates to Hue-Saturation-Value (HSV) coordinates. An example of RGB and HSV decompositions is seen in Figure 1.7.

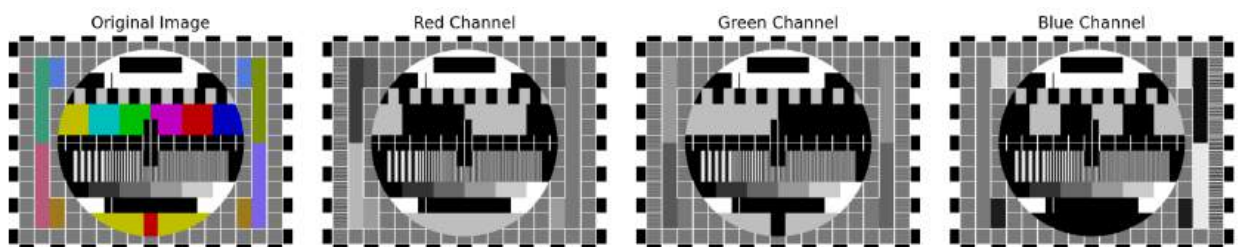


**Figure 1.7** Decomposition of the Phillips circle pattern into its individual red, green, and blue channels, shown in greyscale.

It is easy to see the disadvantages of using RGB coordinates for analysis, as it is not possible to easily discern which regions are colorful, nor what color each region is, from the RGB decomposition alone. Furthermore, nearly all geometric features remain visible in all three decomposition channels. Figure 1.8 shows the same image, but decomposed into HSV coordinates.

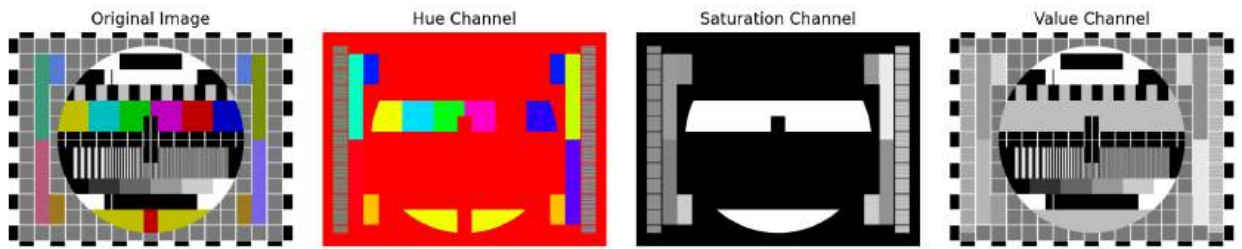


**Figure 1.8** Decomposition of the Phillips circle pattern into its individual hue (shown in true hue), saturation, and value channels (shown in grayscale).

It is easier to see how each individual channel in HSV can serve a specific purpose. The hue channel encodes only information about the color of some part of an image while the other two channels do not encode any information about color. In the case of the Phillips circle pattern, the saturation channel happens to encode information on the larger geometric shapes visible in the image, while the value channel encodes information about the textures in the image. This need not be the case in all images, but it is helpful to note that HSV space has a tendency to help separate different types of information in an image more so than RGB space.

The main advantage of encoding deflection information in the hue channel is that it is independent of the intensity of the light reaching the sensor. This means that the measured deflection is insensitive to changes in opacity of the working fluid, so long as sufficient light is able to pass through the fluid. However, hue is not the information natively gathered by the camera's sensor. An example RGB to HSV conversion is shown below in Eqs. 1:

$$\begin{aligned}
V &\leftarrow \max(R, G, B) \\
S &\leftarrow \begin{cases} \frac{V - \min(R, G, B)}{V} & \text{if } V \neq 0 \\ 0 & \text{otherwise} \end{cases} \\
H &\leftarrow \begin{cases} 60(G - B)/(V - \min(R, G, B)) & \text{if } V = R \\ 120 + 60(B - R)/(V - \min(R, G, B)) & \text{if } V = G \\ 240 + 60(R - G)/(V - \min(R, G, B)) & \text{if } V = B \\ 0 & \text{if } R = G = B \end{cases} \quad (1)
\end{aligned}$$

The main goal of the RGB to HSV conversion is to numerically calculate how bright a light is (value), how colorful that light is (i.e. the distance to an equally bright gray, or saturation), and the color which that light possesses (assuming the light is not gray, or hue), based on the activation of the red, green, and blue channels of an RGB sensor. Value corresponds to the brightness of the brightest RGB channel, that is, a value of zero indicates black, and higher values of value indicate more light making it to the photo sensor. Saturation indicates how far the given pixel is from being grayscale, that is, how definitive the color is.

As shown in Figure 1.9, both high saturation and high value (or in this case intensity) are needed to make a color definitive. Too low of an intensity value results in black (region C), while low saturation values result in white, gray, or otherwise weak colors that become sensitive to small changes in any of the RGB channels (regions A and B). Region D, where color is well defined, is only reachable with sufficiently high saturation and value intensities [18].

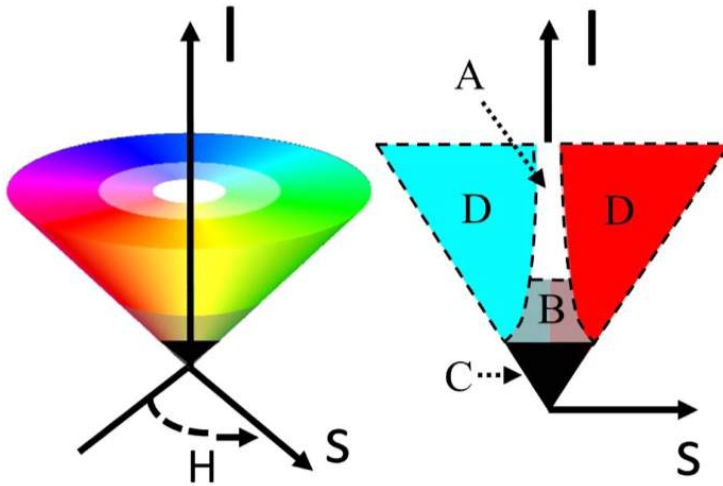


**Figure 1.9** A visual representation of HSV space, with a cross section view [18].

Most quantitative RSD studies focus on using the quantitative hue value in order to gain insight to the density gradients. However, color imaging produces three channels of data (red, blue, and green of RGB). When converting to hue, this also produces values for saturation and intensity, or saturation and value (the S and I or S and V in HSI or HSV, respectively). The S and V channels generally remain unused in most studies, as the hue channel is the one used for quantitative RSD analysis. There are, however, some studies that have made use of the S and V channels, for example to find the liquid penetration length in a diesel injection, with low V values indicating liquid fuel blocking light from reaching the camera [18]. The cool flame detection algorithm presented here specifically makes use of the S and V channels, although to a much greater extent.

It should be noted here that there exist several standards for conversion of image data from RGB to hue representations, such as HSL, HSI, CIELAB LUV and LAB, or CIECAM02 representations. Due to the large quantity of data that required processing in this work, the RGB2HSV routine as implemented by the OpenCV library was chosen, due to its computational

speed when compared to other RGB to HSV implementations found in other common Python libraries. Theoretically, if one were to use mismatched conversion schemes when designing their rainbow filters and processing data, this could lead to issues in data processing. Additionally, the exact color response curve of the camera is unknown, along with pixel-to-pixel variations in color response. These issues are mitigated by the use of calibration curves for each pixel. By assigning each hue on the filter to a “ground truth” deflection distance, as long as the same RGB to HSV conversion is used to create the calibration curves and read experimental data, the exact algorithm used to make the conversion does not matter, so long as the algorithm remains sufficiently responsive to changes in hue along the axis of deflection.

This flexibility is offered by the fact that the change in hue is not an intrinsic effect of the process one is trying to measure, but rather a result of how one is measuring it: because the spatial dimensions of the camera are already encoding spatial information about the phenomenon being studied, angular deflection is encoded in one of the other “free” dimensions on the camera’s sensor, in this case hue; hue is simply a proxy for angular deflection. Because the conversion from angular deflection to hue is entirely artificial, the experimenter has full control over the conversion between angular deflection and hue [16]. This filter design is usually specific to the filter creation and imaging sensors used by each experimenter; Greenberg [16] found very low sensitivity in the blue/cyan range when developing the first quantitative RSD system, while the present RSD setup at the ECL found that hues in the yellow regime are generally compressed. This can arise from difficulties in either manufacture or sensor sensitivity (as the RGB to HSV conversion process is inherently nonlinear), making it difficult to obtain accurate deflection values over certain ranges.

Due to nonlinearities introduced in the design and manufacture of the filter, as well as nonlinearities in the photosensor array and the RGB to HSV conversion, it is important to calibrate the system [17]. This is achieved by mounting the filter to a linear stage and obtaining a series of images of the background flow while the linear stage is advanced across the entire measurement range. A relationship between position along the filter and measure hue can then be established and stored for use when converting hue values back into deflection across the rainbow filter.

## 1.8 Limitations of RSD

Quantitative RSD promises the ability to turn each pixel of the camera into a data point in the flow, however, since only an index of refraction is measured for each data point, one must be able to fix some thermodynamic variables in order to find the full thermodynamic state of the fluid. Thankfully, assumptions can often be made about the flow phenomenon being studied (for example, it might be possible to assume all processes will be isobaric and in the ideal gas regime, fixing temperature) [17]. Because of the existence of two separate combustion modes in diesel combustion, there is no one-size-fits all thermodynamic model or set of assumptions that can be fit to the data. Separate thermodynamic and chemical models must be employed for the mixing (non-combustion), cool flame, and hot flame regimes; as such, a computer program capable of identifying the different regimes is developed.

While the RSD system and CPFR setup promises to offer a great deal of insight into the diesel combustion process, several obstacles exist to making full utilization of the data.

Firstly, the rainbow hue filters and the color sensors of the camera both have inherent imperfections. This is resolved through the use of calibration curves for each pixel on the camera. The Pierce criterion is employed during calibration to identify and discard outlier values

Another issue arises from the fact that the camera can only capture two-dimensional data of a three-dimensional flow field, meaning that each pixel is not simply the index of refraction at a point, but instead the average index of refraction along each light ray. One solution to this problem is to average many injections (on the order of hundreds or thousands of injections), thus creating a truly axisymmetric flow which can then be mapped back to a 3D distribution using an inverse Abel transform [17].

However, the injection-averaging process introduces a new problem: no two injections are identical; in fact, there is a very wide variety in injections [14].

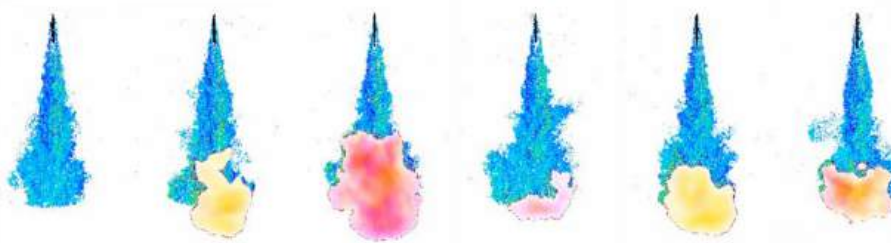


**Figure 1.10** A variety of injections, all at 1.9 ms after injection. Blue-green indicates RSD data, yellow indicates hydroxyl chemical activity, and magenta indicates soot formation.

Figure 1.10 shows several different injections at the same time after injection with chemiluminescence (yellow) and soot temperature (magenta) overlays. Although the same amount of fuel has been injected and at equal conditions for every injection, and all injections are shown at the same time after injection, there is a wide range of combustion evolution present. The process of ensemble averaging many injections leads to multiple fundamentally different combustion regimes being stacked on top of each other. When studying helium jets using RSD, Wanstall [17] noted that “hardware averaging” by taking long exposure RSD images with inherently nonlinear filters leads to erroneous results; similarly, ensemble averaging a large number of injections undergoing inherently nonlinear (even discontinuous) thermodynamic

process will lead to similar issues with regards to applying a simple mean to an inherently multimodal process.

## CHAPTER 2. LITERATURE REVIEW

The main purpose of the new work presented here is to bridge the gap between modelling and experimental studies. As noted in many previous works, bridging this gap remains a difficulty in the field of combustion research [14], especially in extreme conditions. Due to the strong coupling between chemical kinetics and fluid mechanics, as well as highly turbulent conditions, computationally expensive direct numerical simulations (DNS) are required, sometimes needing up to 200,000 core hours or more to complete a simulation [20].<sup>1</sup> Modelling studies require experimental data to verify results, yet large datasets are hard to obtain. The volume of data that is obtained from optical techniques is staggeringly large and requires significant post-processing to convert into usable thermodynamic and chemical properties. Oftentimes, modelling must be used to fill in the gaps in data from experimental studies in order to make the data usable. An interesting development in the field is the use of state estimation techniques, but these often require some form of training data to give accurate results. This section is intended to familiarize the reader with the existing literature on the subjects of cool flames, rainbow schlieren and some related difficulties with implementation, and the wider trends in combustion research. Table 2.1 lists papers relevant to this study, along with some notes on their general area of study. Papers that hold key insights directly affecting the design of the algorithms in this work are described in further depth.

---

<sup>1</sup> i.e., 200,000 hours for a single CPU, or one hour on 200,000 CPUs. In either scenario, this gets expensive.

**Table 2.1** List of articles relevant to this work

Title	Author(s)	Year	Study type	Notes
Conceptual models for partially premixed low-temperature diesel combustion [21]	Mark P.B. Musculus, Paul C. Miles, Lyle M. Pickett	2013	Overview	Conceptual introduction to the structure and evolution of combusting diesel engine sprays, taking into account cool flames.
Understanding cool flames and warm flames [10]	Yiguang Ju	2021	Overview	Overview of the current standing on cool flame research, especially in regards to diesel engines.
A direct numerical simulation of cool-flame affected autoignition in diesel engine-relevant conditions [21]	Alex Krisman, Evatt R. Hawkes, Mohsen Talei, Ankit Bhagatwala, Jacqueline H. Chen	2017	Modelling	DNS of turbulent fuel mixing and ignition at relevant conditions. It is theorized that turbulent mixing energy imparts the kinetic energy needed to ignite the mixture.
Direct numerical simulations of turbulent premixed cool flames: Global and local flame dynamics analysis [11]	Yiqing Wang, Chao Xu, Cheng Chi, Zheng Chen	2024	Modelling	Expands on simulation work by Krisman et al.

Turbulent nonpremixed cool flames: Experimental measurements, Direct Numerical Simulation, and manifold-based combustion modeling [22]	Alex G. Novoselov, Christopher B. Reuter, Omar R. Yehia, Sang Hee Won, Matthew K. Fu, Katherine Kokmanian, Marcus Hultmark, Yiguang Ju, Michael E. Mueller	2019	Experimental and modelling	Comparison of modelling and experimental results for turbulent flames, establishing accuracy of modelling at atmospheric pressure.
An experimental and numerical investigation to characterize the low-temperature heat release in stoichiometric and lean combustion [23]	Muhammad Waqas, Song Cheng, S. Scott Goldsborough, Toby Rockstroh, Bengt Johansson, Christopher P. Kolodziej	2021	Experimental and modelling	Not spatially resolved. Provides a good overview on chemical heat release regimes and evolution for cool flames.
Quantifying liquid boundary and vapor distributions in a fuel spray by rainbow schlieren deflectometry [24]	C Taber Wanstall, Ajay K Agrawal, Joshua A Bittle	2017	Experimental	Examines the liquid fuel penetration using both Mie scattering and RSD residual data (saturation and value from HSV).
Phase boundary detection in transient, evaporating high-pressure fuel sprays by rainbow schlieren deflectometry [18]	C. Taber Wanstall, Ajay K. Agrawal, Joshua A. Bittle	2019	Experimental	Further exploration of the use of RSD residual data to analyze two-phase flow.

Simultaneous rainbow schlieren deflectometry and OH* chemiluminescence imaging of a diesel spray flame in constant pressure flow rig [25]	Allen Parker, C. Taber Wanstall, Shawn A. Reggeti, Joshua A. Bittle, Ajay K. Agrawal	2021	Experimental	Use of ensemble averaging of large numbers of fuel injections and exploration of spatially resolved cool flame behaviour at relevant operating conditions using RSD and other optical techniques.
Quantitative concentration measurements in a turbulent helium jet using rainbow schlieren deflectometry [17]	C. Taber Wanstall, Joshua A. Bittle & Ajay K. Agrawal	2021	Experimental	Studied a helium jet in atmospheric conditions, developing numerical models for quantitative RSD and turbulent mixing.
Comparing Global Spray Combustion Characteristics and Local Shot-to-Shot Variations in a Reacting n-Heptane Spray [26]	Shawn A. Reggeti, Allen Parker, C. Taber Wanstall, Ajay K. Agrawal, Joshua A. Bittle	2021	Experimental	Introduction to difference between ensemble averaging and representative injections.
Representative Phenomena of Cyclic Turbulent Combustion in High-Pressure Fuel Sprays [14]	Allen Parker, Ajay Agrawal & Joshua Bittle	2023	Experimental	Studied variations in injections and comparisons to ensemble average.
Dynamic characteristics of pilot injection: Spray evaporation, mixture formation, and combustion under engine-like conditions [27]	Shiyan Li, Yijie Wei, Ning Wang, Shuai Huang, Xinyi Zhou, Jiale Cao, Run Chen, Tie Li	2025	Experimental	Double-injection fuel setup; results indicate increased cool flame activity.
State estimation in wall-bounded flow systems [28]	Jérôme Hœpffner, Thomas Bewley	2006	State estimation	Introduction to state estimation methodologies for fluid flows.

Physics-informed neural networks for reacting flows: Species reconstruction with finite rate chemistry from sparse and noisy velocity measurements [29]	Fabio Frohberg, Pablo Kandel, Abdulla Ghani	2025	State estimation	Neural networks used to make up for sparse data collection
---	---	------	------------------	--

## 2.1 Representative Phenomena of Cyclic Turbulent Combustion in High-Pressure Fuel Sprays [14]

This is one of the more comprehensive works on the experimental setup and diagnostic techniques used in this paper, as well as the main work that this paper aims to build on. The paper uses RSD, two color pyrometry (soot distribution and temperature measurement), and hydroxyl chemiluminescence (chemical activity measurement) to investigate n-heptane fuel sprays at 800 K and 30 bar. The main focus of the study was on injection-to-injection variation and the applicability of using ensemble averaging to analyze bulk behaviour of the fuel spray and combustion process. Z-scores, indicating the deviation of each injection from the most typical injection, are calculated, and the injections deemed furthest from a typical injection are analyzed and compared with the ensemble average. It is found that these irregular injections are significantly different not only from the ensemble average, but also from each other. Some interesting developments in this paper are the application of z-score methodology to group injections with similar characteristics and the comparison of individual injection analysis with ensemble behaviour. Additionally, the dataset gathered in the representative injection study was the same dataset that was used for testing and validation of the methodology in this paper.

## **2.2 Quantitative concentration measurements in a turbulent helium jet using rainbow schlieren deflectometry [17]**

This paper applies RSD in the analysis of a turbulent helium jet exhausting to ambient conditions. The experimental setup is relatively simple, with a canonical RSD setup and a constant stream of helium exhausting into the atmosphere. The main applications of the paper to this work lie in the methods used to calibrate the RSD system and analyze the helium jet. Equations of diffraction for a conical flow and linear rainbow filter are derived, as well as the use of an inverse Abel transform to convert the Cartesian data gathered by the RSD setup into the cylindrical coordinates of the helium jet. The paper then describes the process of pixel-by-pixel calibration of the rainbow filter by traversing the filter across the focal point of the RSD light beam while the test section has no flow. Quantitative RSD is applied in order to calculate the mole fraction of helium at any given point in the image for every frame, and the results are compared with published values. An interesting note in the paper is the use of “hardware averaging,” that is, using a long exposure in order to gather ensemble average data without the need to “software average” by calculating the arithmetic mean of many frames. However, it was concluded that due to the nonlinearities of the rainbow filter and photosensor affecting the hue to deflection conversion, it is better to “software average” by taking many short exposures, applying the calibrated hue to deflection conversion, and then taking the ensemble average. Other takeaways from this paper include the validation of RSD and the inverse Abel transform to analyze axisymmetric flows with nonuniform chemical compositions, such as flows where mixing occurs.

### **2.3 Phase boundary detection in transient, evaporating high-pressure fuel sprays by rainbow schlieren deflectometry [18]**

This paper is notable in its use of both the saturation and intensity values along with typical hue values associated with RSD analysis. In this case, the intensity value is used to calculate the liquid fuel penetration length in a diesel injection. This is defined as the distance the injected fuel travels as a liquid before it is atomized or evaporates in the high-temperature ambient conditions of the combustion chamber. The general experimental setup and techniques (with some variations in test pressure and temperature) are the same as used in the diesel injection study discussed earlier, as well as the one used for the present work. Data is gathered from multiple injections. The liquid length is detected by detecting a region with lower than some threshold intensity value. It is found that liquid length detection is relatively sensitive to the specific threshold value that is set. Results of the new liquid length estimation methodology are compared to previous methodologies utilizing Mie scattering. Additionally, the methodology presented includes an upper and lower bound on the possible liquid region, implying that the region in between the two bounds is a mixture of both liquid and vaporized phases. The key takeaway from this paper is that although the saturation and value intensities do not hold any direct quantitative impact on the RSD process of converting hue to a deflection value and subsequent calculation of thermodynamics properties, the saturation and value intensities still hold information that can be used to better understand underlying flow structures in the test area of an RSD setup.

## CHAPTER 3. FLOW REGIME CLASSIFICATION ALGORITHM

### 3.1 Introduction

The main goal of this algorithm is, given an RSD image of a diesel injection, to identify the location of the major mixing regimes present in the image. There are several secondary goals: ideally, the algorithm will be background-agnostic, that is, there should be a minimum number of arbitrary threshold values that must be set in order for the algorithm to work. The algorithm should ideally be written in Python, as that is the language that the rest of the data analysis suite is written in. Consistency in language makes the code base more manageable in the long term. Lastly, the algorithm should be relatively fast. As the number of injections can reach into the thousands, the total number of frames to be analyzed can reach into the hundreds of thousands. As such, it is beneficial for the program to be able to run at higher speeds in order to maintain a manageable processing time.

### 3.2 Experimental Setup

The experimental setup used in this work is based on the setup used in previous works by the UA ECL. The concept of operations is described in Chapter 2. For the purposes of software testing, the injection dataset gathered by Parker for use in previous studies [14]. A Bosch CRIN3-18 injector, modified to have a single 100  $\mu\text{m}$  hole at the tip was used to inject n-heptane fuel into ambient conditions of 800 K and 30 bar. The RSD system used an Energetiq EQ-99X fiber coupled broadband light source for illumination, refocused into a point source using two 75mm focal length, 50 mm diameter lenses followed by a 3 mm x 100  $\mu\text{m}$  rectangular aperture to reject any unfocused light. One of the advantages of using a linear filter is that the “point” light source need only be infinitely thin in the direction of filter sensitivity, allowing more light to be passed through the experiment. The collimating and decollimating lenses used were 75 mm

diameter, 250 mm focal length achromatic doublet lenses. The rectangular focusing aperture and rainbow filter were placed at the focal points of the collimating and decollimating lenses, respectively. Light was captured using a Photron Nova S9 color camera equipped with a Nikon Nikkor 50 mm lens at a 512 x 784 pixel resolution, 20 kHz framerate, and 4  $\mu$ s exposure time. This setup resulted in a linear resolution of 90  $\mu$ m per pixel.

### 3.3 Code Requirements

The requirements of writing the analysis in Python while maintaining relatively fast runtimes immediately points to the use of precompiled Python data processing libraries such as Numpy, SciPy, and SciKit. These libraries provide a large number of standard linear algebra, statistical, image filtering and transformation, and basic machine learning capabilities. All of these libraries are well documented open-source projects that are widely used by Python developers. This allows for the easy development of an image processing code. An additional benefit is that these libraries handle many standard processes such as linear transforms, Fourier transforms, and data clustering, allowing the final code to read like a set of high-level instructions while hiding the actual implementation of these algorithms under a layer of abstraction; thus increasing readability.

#### 3.3.1 Code structure strategy

The basic strategy behind the flow region classification algorithm is to pass an image of the injection through a series of filters such that the flow regime of interest (spray, cool flame, etc) is highlighted. The result is a greyscale image of the injection, where the intensity value of each pixel represents how well that pixel or region exhibits properties similar to the flow regime of interest. It is important to note that this value is not a quantitative measure of the probability of that pixel being part of a flow regime, simply a qualitative measure relative to the other pixels in

the image. A threshold value must be set to define which pixels truly are part of the flow regime of interest and which pixels are not. Setting this threshold too high can lead to false positives; setting it too low can lead to false negatives. Some flow regimes may show up in filters intended for a different flow regime, albeit weaker than the target flow regime. As such, results are sensitive to this threshold value. It is impractical for a human to go through the data and set threshold values for thousands of injections. Instead, statistical techniques can be used to identify where the cutoff value should be placed.

Once a “qualitative” image with candidate regimes highlighted is produced, statistical methods can be employed to evaluate the statistical likelihood of each pixel being part of the flow regime in question. Oftentimes it is helpful to view a histogram plot of the image, where the independent variable is the “qualitative” intensity value, and the dependent axis shows the number of pixels with that intensity value, thus displaying a Probability Distribution Function (PDF) of the intensity values. In many cases, the PDF of an image will be a gaussian distribution or mixture of gaussian distributions, with each peak representing a different feature or flow regime. Comparing the PDF of an image with a corresponding “background” image (one with no fuel spray), and calculating the combination of gaussian distributions needed to produce a specific PDF, allows for a threshold value to be set that corresponds to any arbitrary confidence in identification of a feature.

### 3.4 Calibration

Before any data processing can take place, the system must first be calibrated. The process of calibration consists of measuring the hue response of the camera at known deflections. This data can then be reversed, using the hue value to find the exact position on the rainbow filter that the light is passing through. Practically, this means mounting the rainbow filter on a linear stage that

moves in the same direction as the “live” direction as the filter. The linear stage is commanded to drive in small increments, with a number of frames (in this study, 100 frames) taken at each position. The frames at each position are averaged in order to remove any random variation experienced by the sensors. By effectively sweeping the focus point along the filter and collecting color data for each pixel at each position on the filter, a calibration curve is created that takes into account both imperfections in the rainbow filter and the camera sensor itself. This study used 250 positions on the filter. However, the exact number of positions and number of frames at each position is a matter of preference by the experimenter and the noise present in the camera sensor; more data taken (positions and frames at position) increase the accuracy of the calibration curve but result in longer calibration times and larger file sizes.

### 3.5 Software Filters Used

Digital image filters differ from the physical rainbow filters used in RSD in that they are purely used for digital image manipulation. Software filters arise from the field of digital signal processing, and are generally aimed at applying a (series) of discretized mathematical operations to an input image in order to highlight or suppress certain features, or otherwise transform the image (for example, converting between space-domain and frequency-domain). In short, a digital filter can be treated as a mathematical function applied to an image, with all the usual rules of algebraic functions (composition, inversion or lack thereof, differentiation, etc) [30]. A brief overview of the filters used in this paper is given here, however, the methods and goals of image processing and filtering are much broader than what is covered here. While filters for use in color images do exist, many filters are intended for use with grayscale images. However, the greyscale input of each filter need not be the true grayscale, for example, the blue channel of

RGB or saturation channel of HSV may be treated as a grayscale image even though neither is the “actual” grayscale that a human sees.

### 3.5.1 Uniform Filter

A uniform filter is perhaps the simplest filter. A uniform filter consists of calculating the arithmetic mean of a pixel and its neighboring pixels [31]. The number of neighboring pixels taken into account is often referred to as the “size” of such a filter. An example of the effect of a uniform filter can be seen in Figure 3.1.

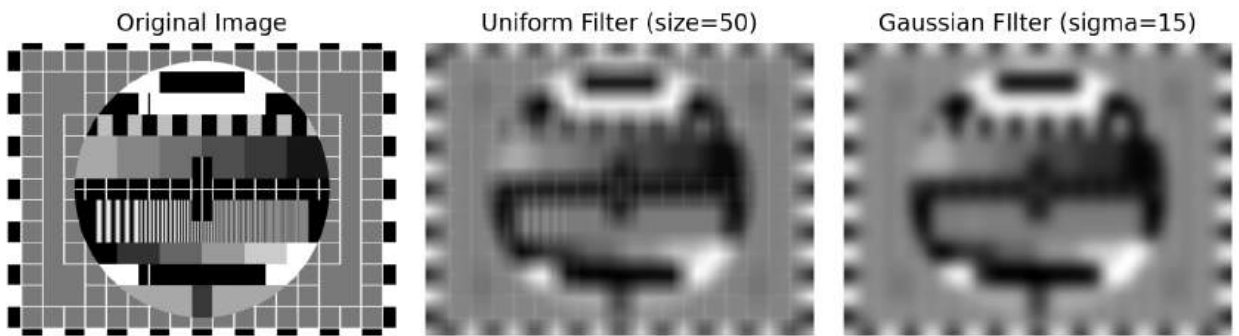


**Figure 3.1** Effect of applying the uniform filter and gaussian filter to the Phillips circle pattern. Note that although the general blurring effect is the same for both filters, the uniform filter better preserves some small scale features such as the background grid.

The main application of the uniform filter in this paper is to calculate the sum of the value of pixels in an area, for example, to count the number of edges in an image where edges have been highlighted. Regions with more edges will appear brighter in the output, while regions with less edges will appear darker.

### 3.5.2 Low-, High-, and Band-pass filters

The goal of low- and high-pass filters is to remove features of either high frequency (rapid changes with respect to the spatial coordinates) or low frequency (steady-state or gradual changes with respect to the spatial coordinates) respectively. Low-pass filters remove small

features, making them useful for detecting larger shapes and forms in an image. High pass filters work in the opposite way, rejecting large shapes and allowing an algorithm to focus on small-scale features. High pass filters are useful in edge detection, where smooth continuities are rejected, while preserving areas with high discontinuities, such as edges [32]. Combining these two filters produces a band pass filter, where only medium-sized features are allowed to pass. Together, these three filters are useful for isolating features of certain sizes [33].

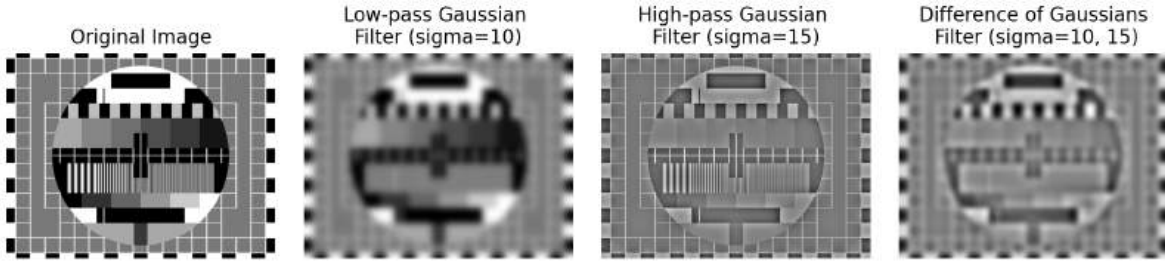


**Figure 3.2** An example of various Gaussian filters applied in low-, high-, and band-pass modes to the Phillips circle pattern.

As seen in Figure 3.2, An intuitive way of thinking about the low-pass filter is as a blurring filter. This effect can be achieved by using a Gaussian filter, where each pixel in the output image corresponds to the weighted average of itself and its neighboring pixels in the input image, with weights corresponding to a multidimensional Gaussian distribution centered on that pixel. The standard deviation of the Gaussian distribution controls the cutoff frequency of the filter. By subtracting a low-pass filtered image from the original, a high-pass filter can be constructed (from a function composition perspective, we can think of this as “low frequencies plus high frequencies equals original image, therefore original minus low frequencies equals high frequencies”). A band-pass filter can similarly be constructed by computing the difference of two Gaussian-filtered images with different cutoff frequencies [34].

### 3.5.3 Erosion

The basic operation of erosion is to make bright zones smaller. It is typically applied to binarized images, that is, to images that consist of pure white and black pixels, however, it can also be applied to grayscale images. The basic premise underpinning either case is that for every output pixel, the lowest brightness value in the neighborhood of that pixel is chosen as the output value. In this way, pixels that are surrounded by other bright regions remain bright and dark pixels that are in dark regions remain dark. However, pixels that are in regions that are partially light and partially dark are outputted as dark, therefore producing the effect of shrinking bright areas and enlarging dark areas, hence the name [35]. Figure 3.3 shows examples of erosion applied to both a binarized and a grayscale image.

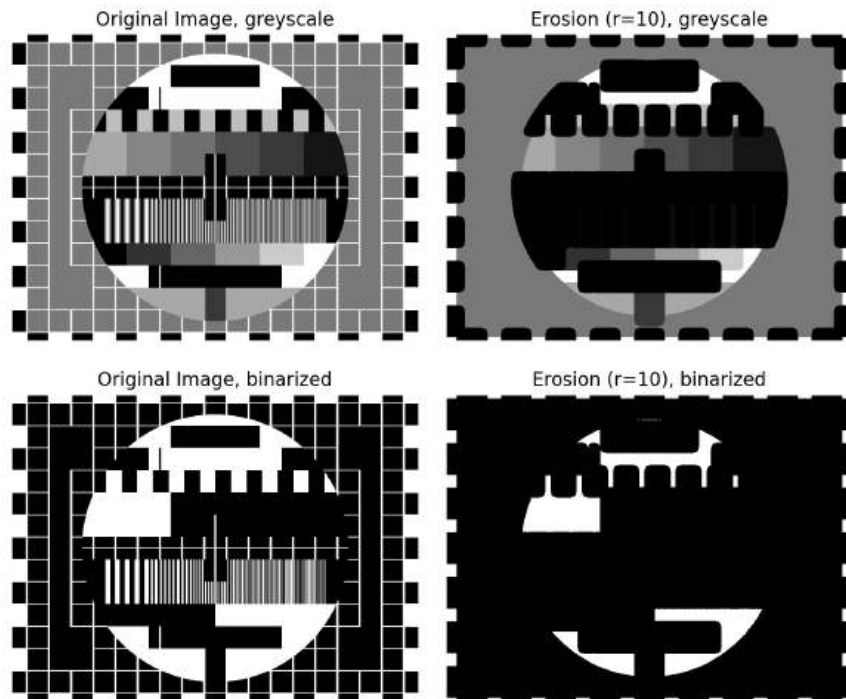


**Figure 3.3** Examples of image erosion on both greyscale and binarized versions of the Phillips test pattern.

### 3.5.4 Dilation

Dilation can be seen as an opposite to erosion, making bright areas larger and dark areas smaller. The filter works by selecting the maximum value in the neighborhood of a pixel as the output value. However, it should be noted that dilation cannot perfectly reverse erosion and vice versa. Both filters are capable of removing small features in an irreversible process. Figure 3.4 shows the effect of dilation on both a binarized and grayscale image [35].

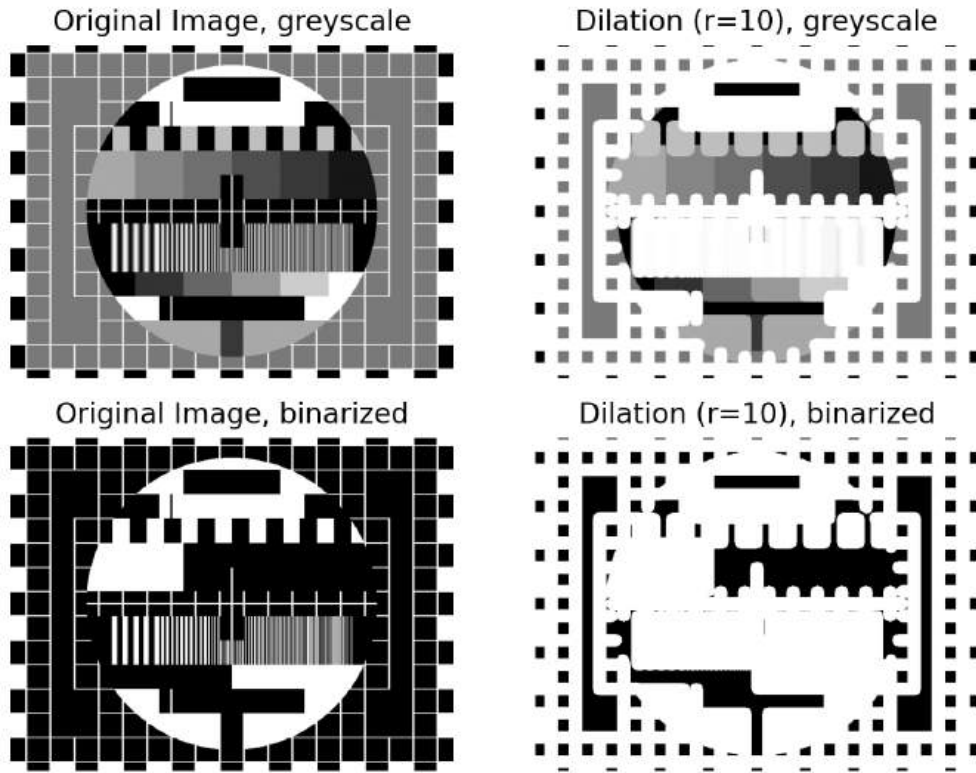


**Figure 3.4** Examples of image dilation on both greyscale and binarized versions of the Phillips test pattern.

### 3.5.5 Area opening

As noted previously, erosion and dilation are not perfect inverses. By applying an erosion followed by a dilation, one achieves area opening. Area opening acts to smooth out bright areas, removing small bright spots and sharp corners while preserving the general size and shape of

bright spots. The output size of bright spots is generally slightly smaller than in the input, due to the smoothing of corners [35]. An example of area opening is shown in Figure 3.5. One application of the area opening filter is to “break apart” several bright regions that are only weakly connected by a small number of pixels. Such an operation is helpful in image segmentation, where regions that should be seen as independent of each other are erroneously connected by a small “bridge,” leading to issues in detecting the two regions as separate.

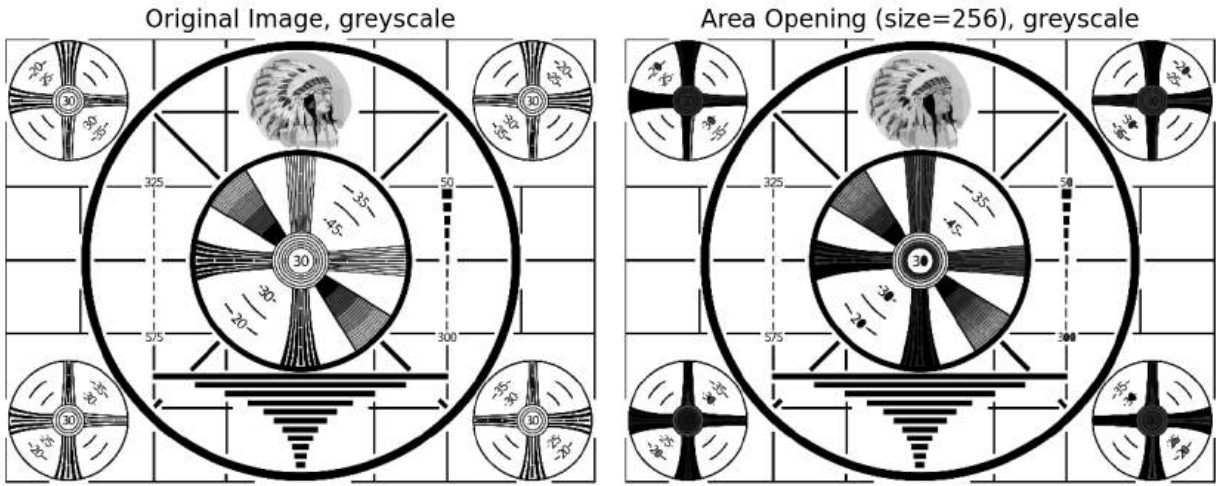


**Figure 3.5** An example of area opening using the RCA "Indian Head" Test Pattern. Note that regions with many small details are merged into larger blocks with roughly the same shape and size as the original.

### 3.5.6 Area closing

Area closing is similar to area opening, but works to remove sharp corners in dark regions, thus breaking apart weakly connected dark regions. It is achieved by performing a dilation followed by an erosion [35]. An example is shown in Figure 3.6.

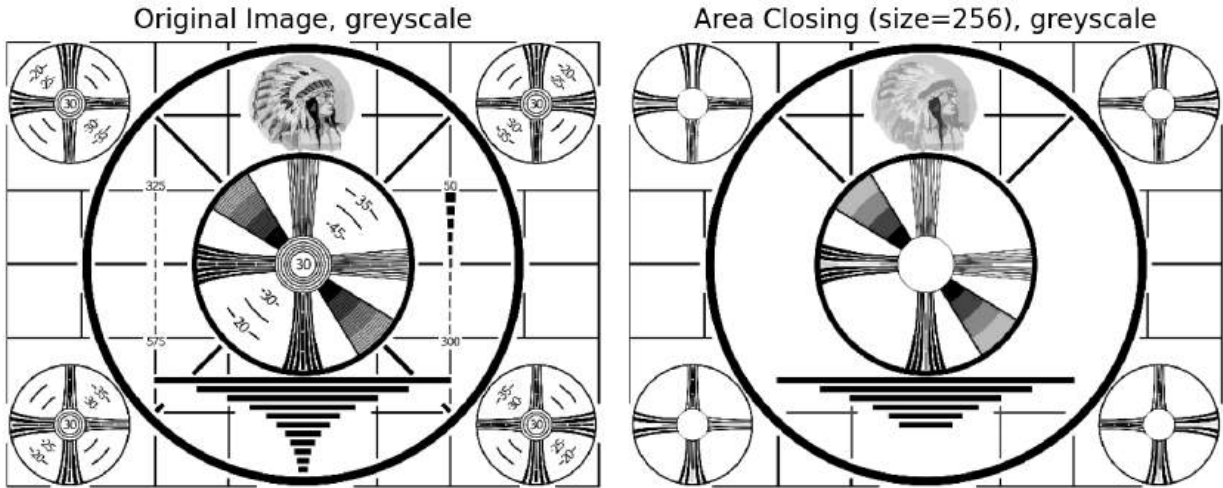


**Figure 3.6** An example of area closing using the RCA "Indian Head" Test Pattern. Note that small features are removed (such as text and the small horizontal bars at the bottom), while larger features are preserved (such as the large horizontal bars).

### 3.5.7 White Top Hat

A white top hat filter is used to extract small features from an image. It does so by subtracting an area opening of an image from the original image. Since an area opening preserves large bright structures while rejecting small bright structures, subtracting an image containing only large structures from the original image will result in an image containing only small structures [36]. An example is shown in Figure 3.7.

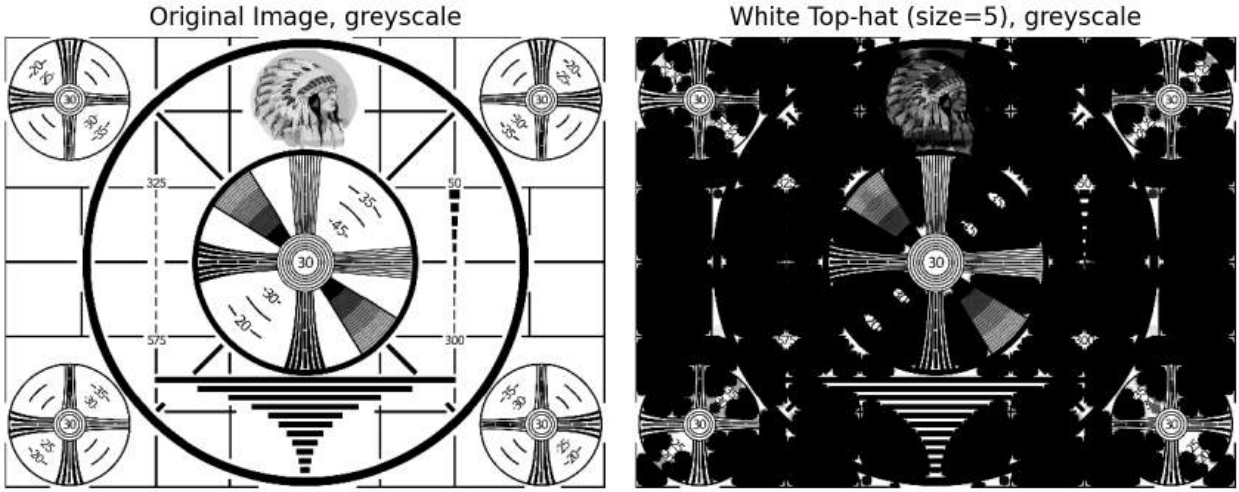


**Figure 3.7** An example of the white top hat filter using the RCA "Indian Head" Test Pattern. Note that the filter extracts only small details (such as the test lines), while rejecting larger structures such as the large rings and grid.

### 3.6 Multimodal Distributions

Multimodal distributions are probability distributions with multiple modes, that is, with multiple peaks. In Figure 3.8, A classical unimodal gaussian distribution is compared with a multimodal distribution resulting from the summation of several Gaussian distributions.

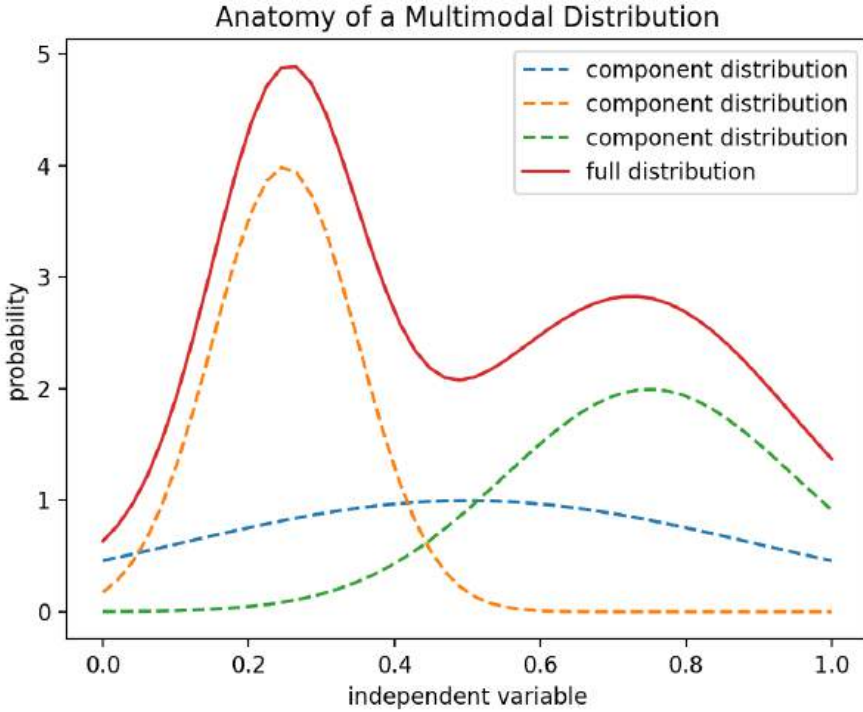


**Figure 3.8** Anatomy of a multimodal distribution. Many multimodal distributions can be broken up into multiple unimodal distributions, especially those multimodal distributions which result from the measurement of multiple phenomena happening simultaneously.

Multimodal distributions prove to be harder to analyze than unimodal distributions due to the fact that they cannot be categorized by a single peak or standard deviation. However, some multimodal distributions can be assumed to be a mixture of Gaussian distributions, that is, they are the result of taking the sum of several gaussian distributions with differing means and standard deviations. The fields of machine learning, specifically the problem of classification, have spent much time developing mathematical models for separating mixed distributions. The algorithms used here, while well established in their respective fields, their detailed explanation is far outside the scope of this paper [37]. The key takeaway is that a mixture of distributions can be broken into an arbitrary number of individual unimodal distributions, which can then be analyzed individually.

### 3.7 Spray/Hot flame detection

The hot flame and spray detection algorithm is relatively simple. It is relatively similar to the techniques used by Wanstall and Bittle for liquid penetration detection [18, 24], though this method extends the methodology to much weaker changes in saturation. An example color image of fuel spray and hot flame can be found in Figure 3.9, alongside the isolated saturation channel of that image.

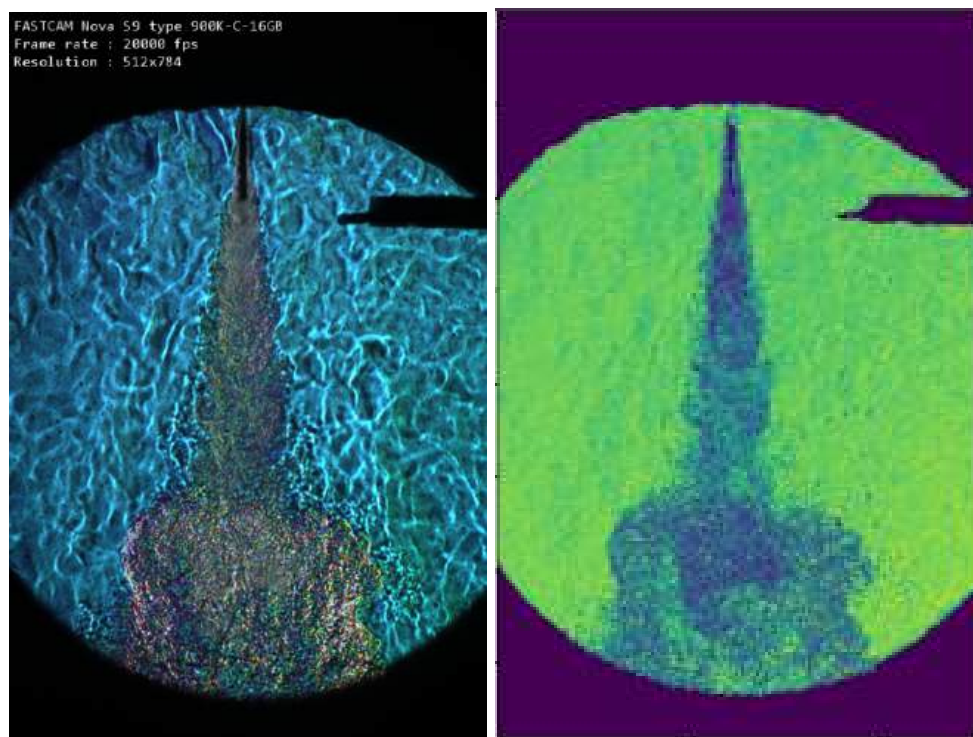


**Figure 3.9** Comparison of true color (left) and isolated saturation (right, yellow/blue scale) RSD images at 3.5 ms after injection for an n-heptane spray at ambient conditions of 800 K and 30 bar.

As can be seen, not much further filtering is needed to highlight the spray and hot flame. Figure 3.10 compares the histograms of the spray image to a “neutral” frame where only the background is visible. A histogram shows the probability distribution function of an image, that is, it shows the probability of any pixel having a specific value. The histogram plot of the

“neutral” frame closely resembles a gaussian. By finding the mean and standard deviation of this distribution, a cutoff value can be found that filters between pixels that are statistically likely to be a spray/hot flame pixel and background pixels, with any arbitrary statistical significance. The standard 95% confidence interval (two standard deviations) was found to be sufficient for these purposes.

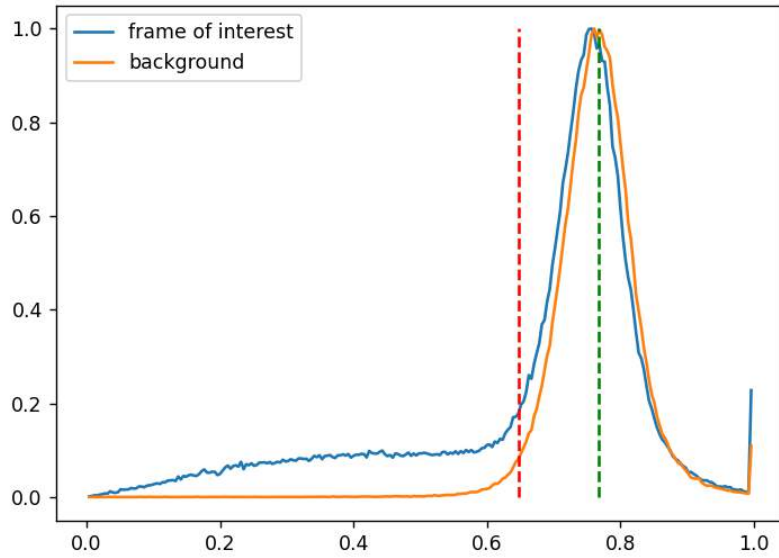


**Figure 3.10** Comparison of histogram plots of the injection saturation image shown in Figure 3.9 (blue) and an image with no spray visible (orange). The green dashed line shows the mean of the background saturation distribution, while the red dashed line represents a threshold cutoff value located two standard deviations from the mean of the background saturation distribution. The x-axis shows saturation value, while the y-axis shows the count of pixels exhibiting the given saturation value. Axis units are arbitrary.

However, directly generating a binary mask from the threshold value does not result in a particularly clean result. There are many “speckles” of false positives and false negatives throughout the image. At this point, the white tophat, dilation, area closing, erosion, and area opening filters are applied to clean up the image. The overall effect of these filters is to remove any small areas of false positives or negatives while preserving the shape of fine flow structures.

The cleaned mask can then be applied to the original image in order to extract just the spray and hot flame region, as seen in Figure 3.11:

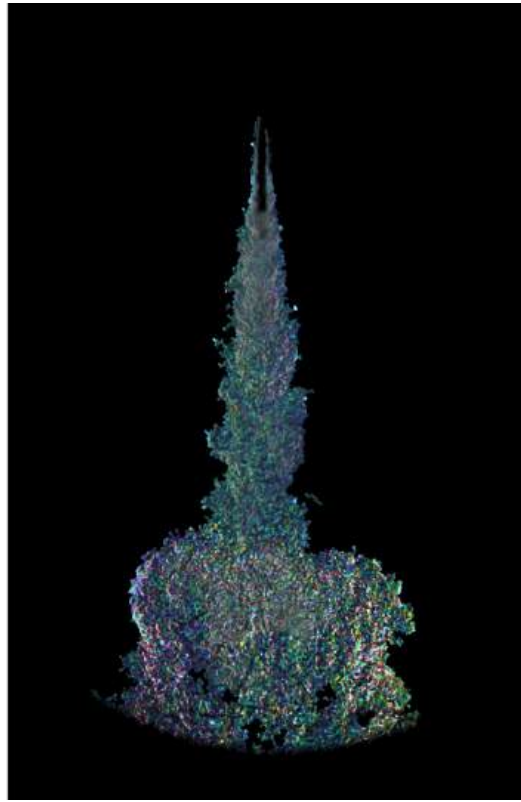


**Figure 3.11** RSD image of isolated spray/hot flame at 3.5 ms after injection, 800 K and 30 bar ambient conditions.

### 3.8 Cool Flame Detection

One of the difficulties with cool flame detection is that the cool flame region has a density similar to the background chamber gas. Because of this, the cool flame region appears to look like the background gas in the hue channel, but is in fact chemically and thermodynamically distinct from the background gas. This offers an example of a case where thermodynamic models cannot be developed based on density gradient alone; rather, more knowledge must be gathered about the flow region the thermodynamic model is being applied to (for example, whether a region is the background or a cool flame). Figure Figure 3.12 shows an example sequence of

images containing a cool flame. Although the circled region at  $t=1.95$  ms is the same color as the background region, there is clearly fuel in the mixture there, indicated by the presence of unburned fuel and hot flame before and after the center frame, respectively.

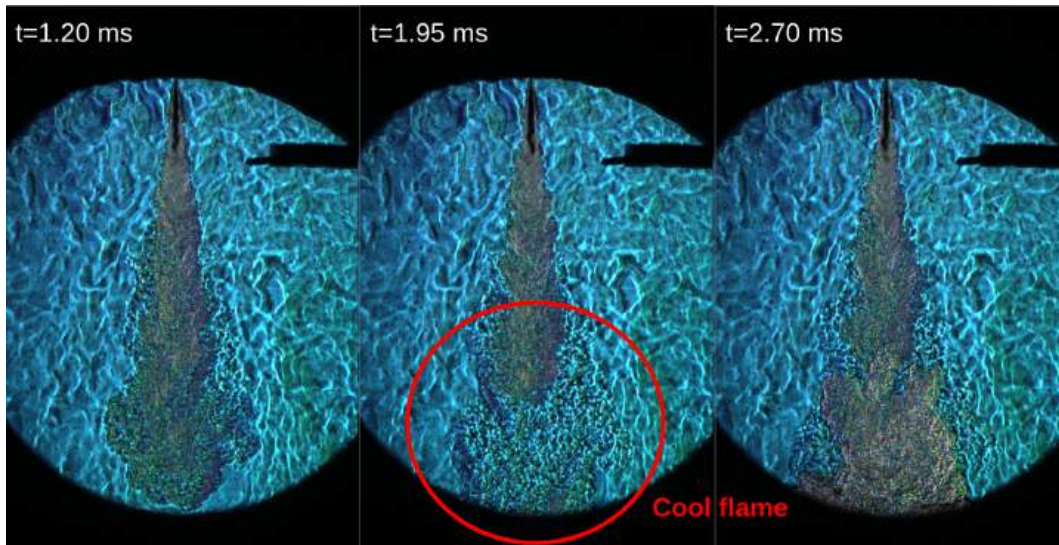


**Figure 3.12** A chronological series of RSD images of an n-heptane at 800 K, 30 bar ambient conditions. The lower part of the fluid spray (circled in the middle frame) seems to "disappear" and then "reappear" as a hot flame at  $t=2.70$  ms. This intermediate step, where the refractive index of the circled regions happens to match the background refractive index, is the cool flame region, as it appears chronologically between the non-reacting and hot flame flow regimes.

By closer inspection of the frame at  $t=1.95$  ms of Figure 3.12, we see that although the background and cool flame regions both have similar hue, the textures of the two regions are distinct from each other, as seen in Figure 3.13. A strategy emerges to target the high-frequency variations that are present in the cool flame but not in the background.

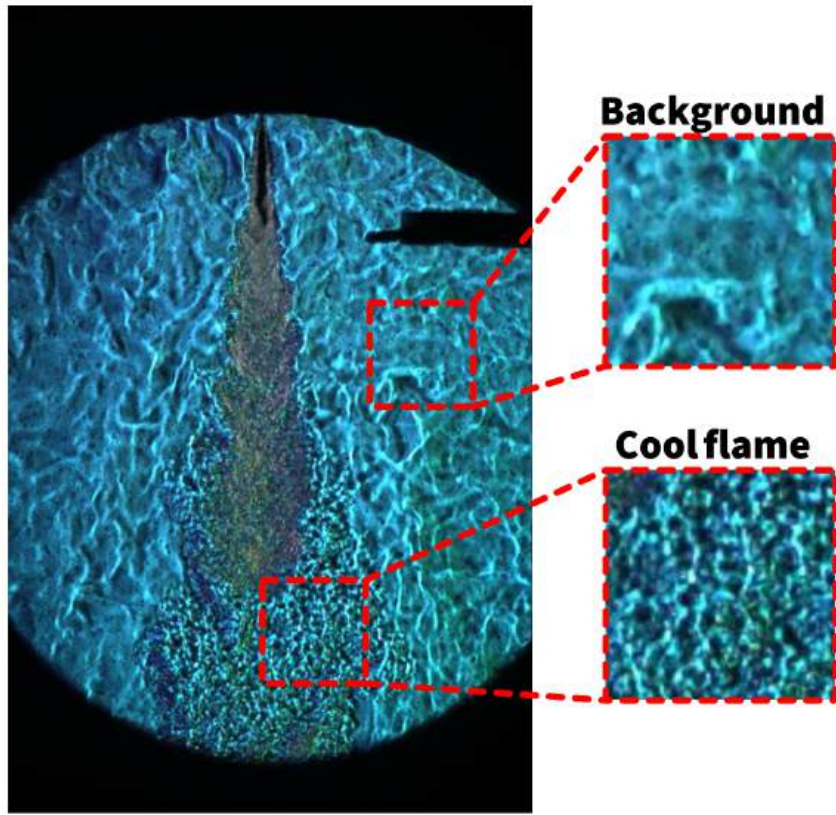


**Figure 3.13** Detail of Figure 3.12 at  $t=1.95$  ms, highlighting the similarities and differences in the background and cool flame regions.

This change in texture is most noticeable in the value channel. Similarly to the process used to derive the spray/hot flame filter, we will start with the  $t=3.5$  ms frame and isolate the value channel from HSV space, as seen in Figure 3.14.

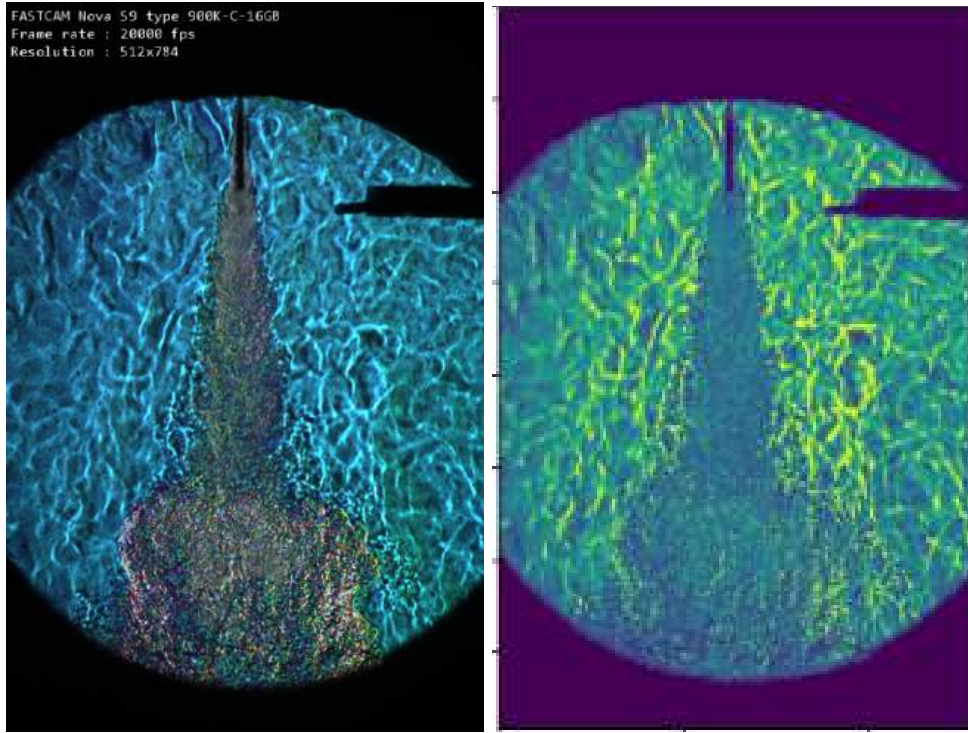


**Figure 3.14** Comparison of true color (left) and isolated value (right, yellow/blue scale) RSD images at 3.5 ms after injection for an n-heptane spray at ambient conditions of 800 K and 30 bar.

Inspecting the image of the value channel, it can be seen that the cool flame region exhibits a texture that is different from the background flow. By applying a high-pass filter, the ripple features of the textures can be highlighted, while rejecting steady-state changes. Applying a uniform filter to the high-pass image then merges areas with ripples; regions with more ripples show up brighter in the blurred image than regions with less ripples. Because a high-pass filter followed by a low-pass filter results in a band pass filter, a difference of gaussians filter is used in practice to process both the edge-detection and edge-counting in a single step. The results of this can be seen in Figure 3.15.

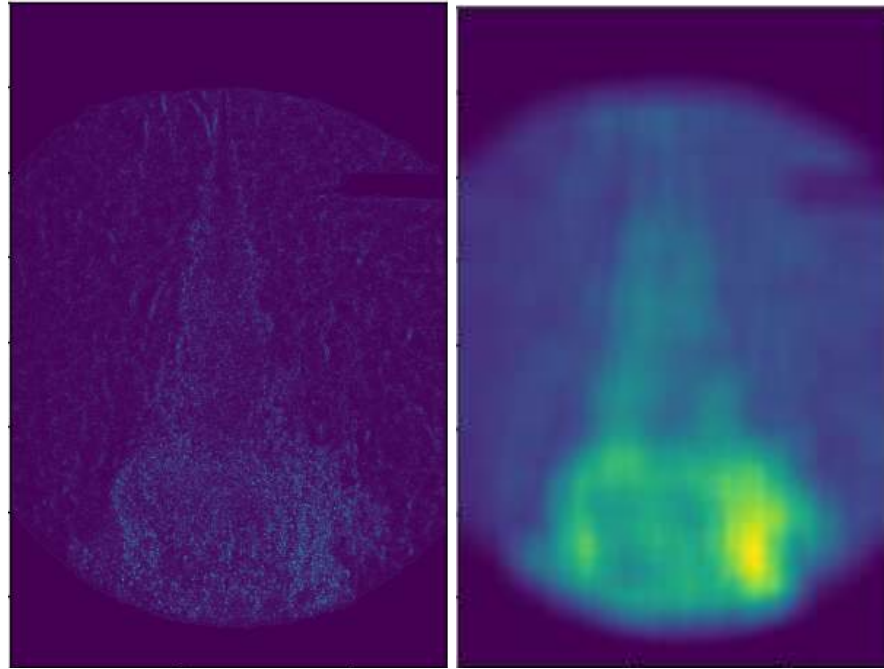


**Figure 3.15** Results of applying a difference of gaussians filter (left) to the value channel image obtained in Figure 3.14, followed by applying a uniform filter to produce a value edge count intensity (right).

A uniform filter is then applied to count the number of edges in the neighborhood of each pixel. Pixels that are closer to a large number of edges or other high-frequency zones are generally more likely to be part of the cool flame region; pixels that are on average further from regions with many edges are more likely to be the background. The effect of the uniform filter applied to the results of the bandpass filter can be seen in Figure 3.15. For lack of a better name, the output of the uniform filter will be referred to as the value edge count intensity. We then construct a histogram of the value edge count intensity, shown in Figure 3.16.

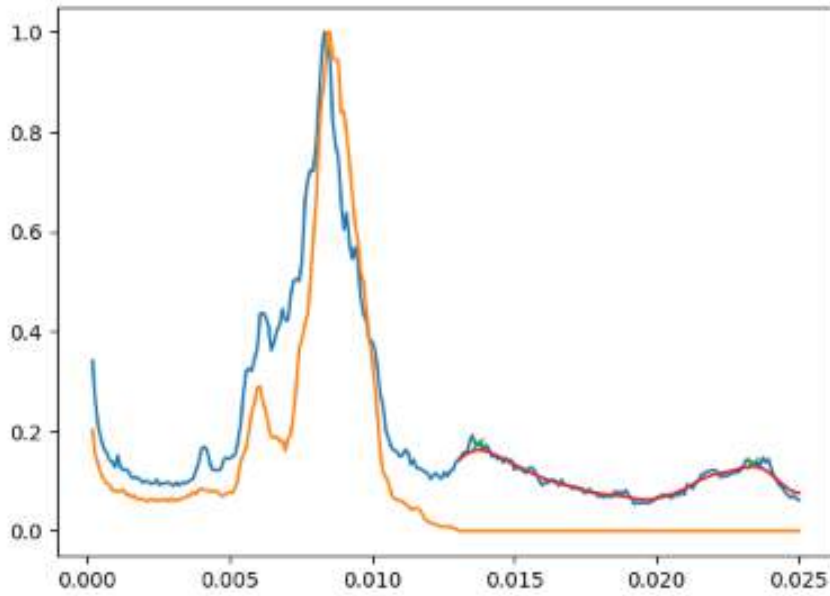


**Figure 3.16** Histogram plot comparison of background edge count value intensities (orange) and spray edge count value intensities (blue,  $t=3.5$  ms). The x-axis is proportional to the number of edges within a given region, while the y-axis represents the count of pixels that have that number of neighboring edges. The units of both axes are arbitrary. Note that the range of edge counts corresponding to the background (left half of the graph) does not follow any simple Gaussian patterns. The right half of the graph, corresponding to edge densities only found in frames with an injection, has a shape that may be a mixture of gaussians. The red line is a smoothing of this region that is used to estimate the number of peaks needed for the mixture of Gaussians method.

Inspecting the histogram plot (Figure 3.16), we find that it has several peaks and does not seem to follow any simple distribution. The left-most peaks, those of lower intensities, correspond to the background flow. The remaining peaks correspond to cool flame and spray/hot flame. Firstly, all pixels that have intensity values within the range of intensities found in the background can be immediately excluded as part of the background. The remaining distribution is considered for the cool flame. A cool flame can generally only exist if there is a fuel spray present from which to feed the cool flame. As such, if the remaining distribution is unimodal, it

can be inferred that no cool flame is present (as any cool flame image will contain at least some fuel spray, forcing two peaks instead of one), and the current frame can be discarded.

In the case of a multimodal distribution, SciKit Learn's Mixture of Gaussians method is used to calculate the means and standard deviations of the peaks. The mixture of gaussians method requires the number of peaks as an input. This is calculated by applying an aggressive gaussian smoothing filter to the remaining portion of the distribution before applying SciPy's `find_peaks()` function to count the number of local maxima. The smoothing is required to prevent `find_peaks()` from detecting false local maxima due to noisy data. The peak with the lowest intensity value is assumed to correspond to the spray/hot flame region, while the peak with higher intensity values corresponds to the cool flame region. In some cases, three or more peaks may be observed. In the case of more than two peaks, it is assumed that only the peak with the highest intensity is the cool flame.

Because we now have several statistical distributions with means and standard deviations to work with, we can define any arbitrary statistical likelihood that a certain cutoff value is or is not part of the cool flame. A threshold value edge count intensity is selected such that there is 95% confidence that a given cool flame pixel is indeed part of the cool flame. Once a threshold value is selected, it can be used to create a binary mask that can be used to extract the cool flame region, as shown in Figure 3.17.

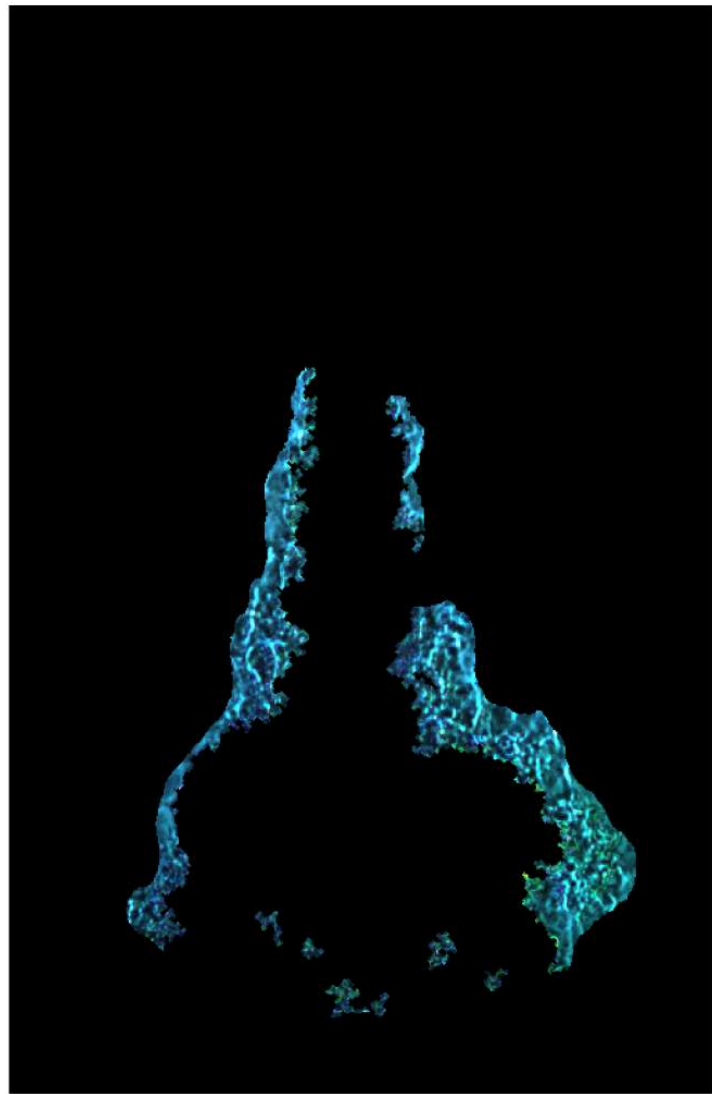


**Figure 3.17** RSD image of isolated cool flame at 3.5 ms after injection, 800 K and 30 bar ambient conditions.

The blurring effect of the uniform filter has several impacts on the application of the cool flame filter. One benefit of this effect is that it automatically removes the small false positive and false negative regions encountered while processing the spray and hot flame. This removes the need for the white top hat, area opening, erosion, dilation, and area closing filters. However, this blurring effect comes with drawbacks: the cool flame detection algorithm is able to capture the shape of the cool flame well, but struggles to resolve individual pixel scale features. Because of

the texture-based approach for the cool flame detection algorithm, there is not a good workaround for this problem; a texture, by definition, must be a feature that consists of many pixels, meaning that pixel-scale resolution with texture detection is likely infeasible.

### 3.9 Implementation

Due to the size of datasets involved (often running into the dozens and possibly hundreds of gigabytes), it is important to consider factors such as processing time and memory usage. As of the time of writing, higher-performance computers (such as those intended for scientific or video editing use) contain enough RAM to hold and process 100+ gigabyte files in memory, many consumer-grade computers still do not possess this capability. Additionally, while the largest file used in this study was roughly 40 GB, there is no theoretical upper limit on the size of experiment data files. These issues can be resolved (or at least alleviated) by the use of parallelization. While parallel processing does not inherently alleviate the issue of data usage (in fact, parallel processing typically requires more memory than a single threaded process), the process of designing an algorithm to run as multi-threaded results in an architecture where it is easier to control memory usage. However, nearly all modern CPUs offer multithreading capabilities. While GPU based processing might offer further improvements in code runtime, the use of GPUs was not investigated for this study.

The end goal of analysis, as in previous studies by Parker [15], is to obtain an ensemble-averaged sequence of time-resolved images. It is helpful to visualize the input data as a grid of images, with one axis representing the elapsed time after start of injection, and the other axis representing the injection number within the ensemble. Although data is collected in a time-series manner, each ensemble average is actually independent of the frame that becomes before or after it in the time sequence. As such, we assign each parallel thread worker to an

ensemble of frames. Each worker only reads the frames it is assigned to, and releases all frames it has read from memory once it computes the ensemble average of the frames it has been assigned. In this manner, the majority of the file remains in storage at any given time, allowing the program to process data files that may exceed the size of available memory.

Each thread worker is given the following tasks. First, the worker is given an ensemble number to analyze. The worker then reads relevant header information from the raw data file (namely the total number of injections, number of frames per injection, and video dimensions). Two three dimensional arrays are pre-allocated (one for the cool flame and one for the spray/hot flame), with dimensions corresponding to the width, height, and total number of frames to be analyzed by the worker. The worker then enters a loop for each frame in the ensemble. Each frame is read into memory from storage, converted to HSV, and pixels with saturation or value numbers that result in very weak color are discarded (i.e. where hue begins to become a function of RGB sensor noise). The cool flame detection and spray/hot flame algorithms are then applied, resulting in binary masks that can be used to select either region. Some areas may have been claimed as both cool flame and spray/hot flame. Because the spray/hot flame algorithm has higher resolution than the cool flame algorithm, the spray/hot flame classification is given precedence over cool flame (i.e., regions marked as true for cool flame and spray are considered to be spray-only). Hues are then converted to deflection angles. It is important that this step is completed before the frames are averaged, due to the nonlinear nature of the hue to angle conversion. Each image, represented as two matrices of deflection angles, one for the cool flame and one for the spray/hot flame, is then added to the pre-allocated ensemble image matrices. The mean and standard deviation of each matrix is then calculated and returned. This process is repeated for each ensemble number.

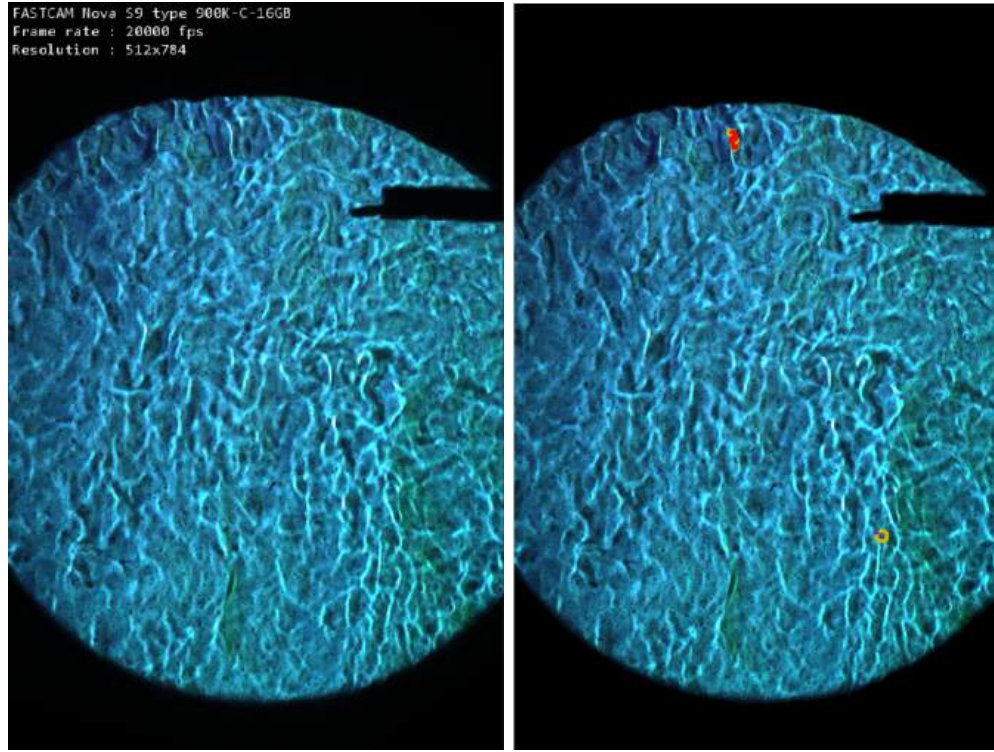
The full list of external Python libraries used is Numpy for array manipulation and analytical tools; SciPy, Scikit-Image, and OpenCV for image manipulation and analytical tools, Scikit-Learn for the calculation of Gaussian mixtures; Matplotlib for visually displaying data; Pool for parallel processing; and TQDM for tracking parallel processing progress.

### 3.10 Results

The cool flame and spray/hot flame detection filters developed in this paper are applied to a sample n-heptane fuel injection at ambient conditions of 800 K and 30 bar, at an exposure time of 4  $\mu$ s and spatial resolution of 90  $\mu$ m per pixel. Figure 3.18 shows the ambient background on the frame in which the injection starts, as well as an image with contours marking the fuel spray/hot flame and cool flame regions. Since there is no fuel spray visible at this point, we would expect that neither filter detects anything. However, a small region of spray (near the injector at the top of the image) and a small region of cool flame (near the bottom-right) are detected.<sup>2</sup>

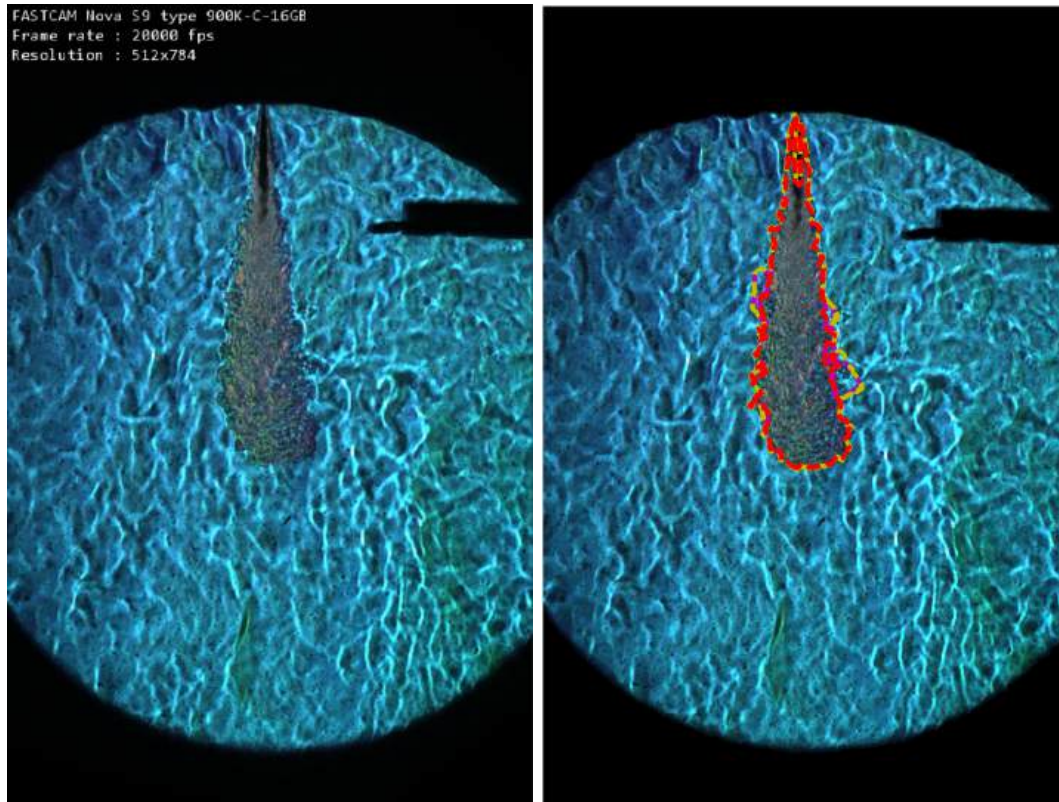
---

<sup>2</sup> It should be noted that the black object in the upper right is a thermocouple used to monitor chamber conditions, while the injector itself is positioned at the edge of the field of view at the center top of the image.



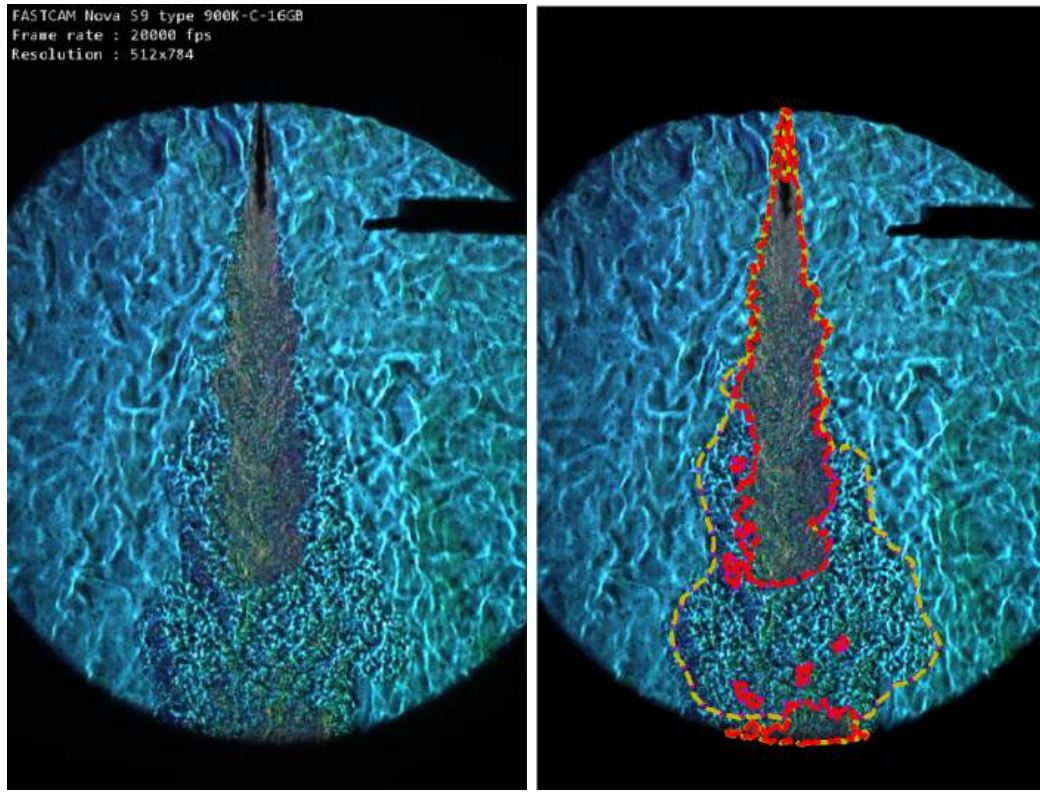
**Figure 3.18** Comparison of input RSD image (left) and cool flame and spray/hot flame contours found by the detection filters (right). Spray and hot flame are shown in red, while cool flame is shown in yellow. Image taken at 0 ms after start of injection.

Figure 3.19 shows an example of filter usage near the beginning of an injection, before the fuel has had enough time to ignite. The spray/hot flame filter (red) identifies the contours of the spray, while the cool flame filter (yellow) identifies a small region near the bottom right of the spray that could be the beginning of a cool flame.



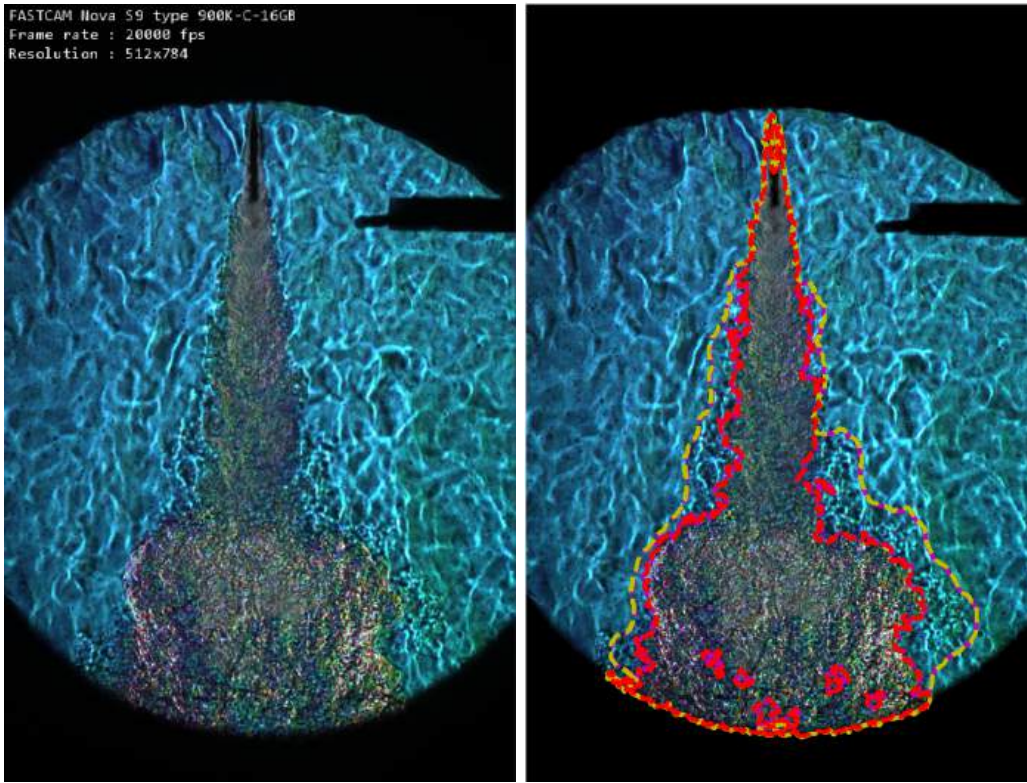
**Figure 3.19** Comparison of input RSD image (left) and cool flame and spray/hot flame contours found by the detection filters (right). Spray and hot flame are shown in red, while cool flame is shown in yellow. Image taken at 0.45 ms after start of injection.

Figure 3.20 shows an example of filter usage on an RSD image with a large cool flame region. The spray/hot flame filter covers the part of the fuel spray near the injector that is still too cold to ignite (the injector and fuel lines are externally cooled), as well as the beginnings of a hot flame near the bottom of the image. The cool flame filter identifies the large cool flame region present below the fuel spray.



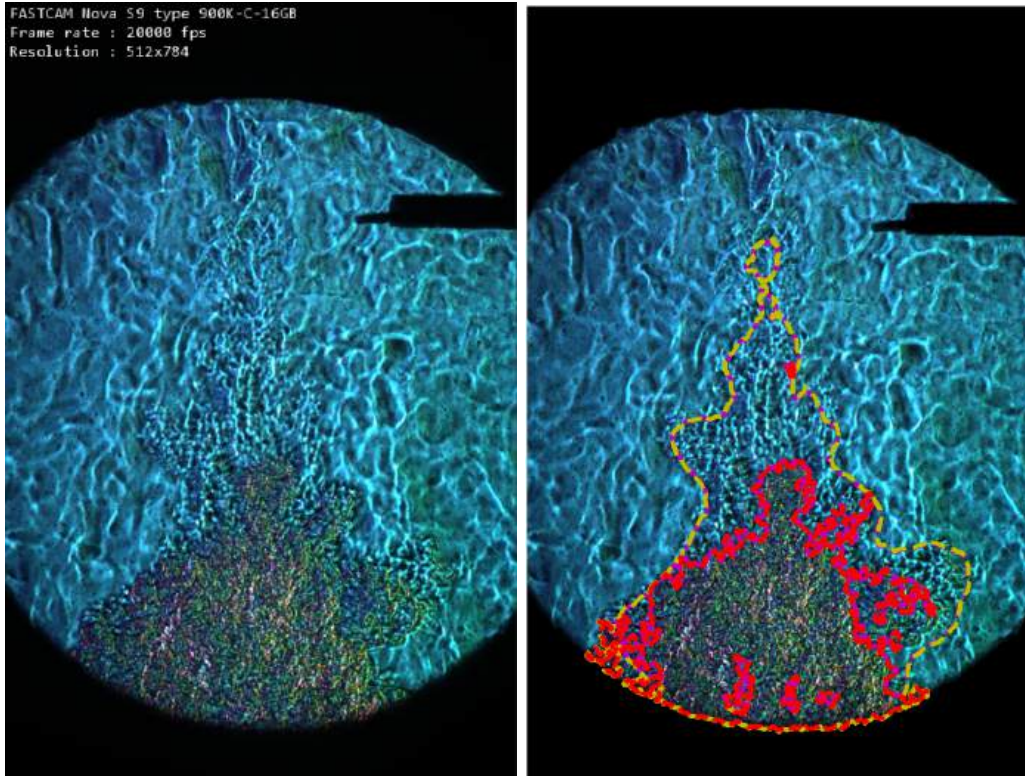
**Figure 3.20** Comparison of input RSD image (left) and cool flame and spray/hot flame contours found by the detection filters (right). Spray and hot flame are shown in red, while cool flame is shown in yellow. Image taken at 1.95 ms after the start of injection.

Figure 3.21 shows an example RSD image of a spray well after ignition, when the image is dominated by the hot flame in the bottom half of the image. There are still small amounts of cool flame being detected near the edges of the fuel spray (center left) and some parts of the hot flame (bottom right).



**Figure 3.21** Comparison of input RSD image (left) and cool flame and spray/hot flame contours found by the detection filters (right). Spray and hot flame are shown in red, while cool flame is shown in yellow. Image taken at 3.2 ms after start of injection.

Figure 3.22 shows an example RSD image taken after the end of injection while there is still burning fuel present in the chamber. The spray/hot flame filter detects the mass of burning fuel that is still in the main combustion region, while the cool flame filter detects the remnants of the fuel spray as it transitions to the cool flame regime.



**Figure 3.22** Comparison of input RSD image (left) and cool flame and spray/hot flame contours found by the detection filters (right). Spray and hot flame are shown in red, while cool flame is shown in yellow. Image taken at 6.2 ms after start of injection.

### 3.11 Discussion

The spray/hot flame and cool flame detection filters perform to their desired specifications, correctly identifying their respective flow regions. Room for improvement still remains; for example with rejecting the two false combustion regions in the background flow in Figure 3.18. However, this can likely be addressed by setting a minimum total area requirement that must be met before an image can be said to have flow in it. The spray/hot flame filter shows surprisingly high fidelity, identifying the flow shape down to a pixel-by-pixel level. Future work may include exploring Krisman et al.'s hypothesis on the link between turbulent mixing and flame seeding by applying correlational tools to the spray mixing and cool flame data gathered in this study [20].

## CHAPTER 4. RECAPITULATION AND CONCLUSIONS

Diesel combustion offers an interesting intersection of turbulent flows, high temperature and high pressure gas and chemical behaviour, unsteady combustion, and strict constraints on allowable combustion products, all while trying to maximize the thermodynamic work done by the combustion process. Thus, thorough investigation and understanding of the processes controlling the mixing, ignition, and combustion of the fuel becomes of great importance both in attempts to select new fuels and design new fuel injectors and injection schemes, as well as in efforts to simulate and model the combustion process, especially when simplifying and validating expensive DNS simulations.

RSD offers great insight into the structure of fuel mixing and combustion by supplying a non-intrusive optical technique with high temporal and spatial resolution at the cost of measuring a variable (index of refraction) that is only weakly linked to the thermodynamic properties of the medium being studied.

The work presented here aimed to separate the various mixing and combustion regimes found within an RSD image, allowing specialized refractive index to thermodynamic property conversion models to be applied to each region, increasing the accuracy of thermodynamic data gathered through RSD methods. This detection and separation was done using a series of image processing filters available through common Python image processing libraries. Statistical analysis of the images and intermediate filtered images is used to select threshold values for the detection of various flow phenomena. Finally, the process is applied to a set of test images, showing that the developed filters properly detect their intended flow regimes.

Future work in this area includes improving the fuzzy “texture detection” cool frame algorithm, combining the flow regime separation with thermodynamic models, and testing the filters over a wider range of operating conditions and fuel types.

## REFERENCES

- [1] Roache, P.J., "Verification of Codes and Calculations," AIAA Journal, Vol. 36, No. 5, May 1998, pp. 696-702. <https://doi.org/10.2514/2.457>
- [2] Ruschmeyer, K., Berndt, B. & Rulfs, H. "The potential of extremely high cylinder pressures in diesel engines." MTZ ind. 2, 64–71 (2012). <https://doi.org/10.1365/s40353-012-0042-9>
- [3] Wanstall, C. Taber, Joshua A. Bittle, Ajay K. Agrawal; "Transient mixing behavior of a supercritical fluid injected into supercritical and subcritical environments." Physics of Fluids 1 February 2022; 34 (2): 023104. <https://doi.org/10.1063/5.0072291>
- [4] Pickett, L., Genzale, C., Bruneaux, G., Malbec, L. et al., "Comparison of Diesel Spray Combustion in Different High-Temperature, High-Pressure Facilities," SAE Int. J. Engines 3(2):156-181, 2010, <https://doi.org/10.4271/2010-01-2106>
- [5] Khair, Magdi K., and W. Addy Majewsky. *Diesel emissions and their control*. SAE International, 2006.
- [6] Heywood, John. *Internal combustion engine fundamentals*. McGraw-Hill Education, 2018.
- [7] Reif, Konrad. *Diesel Engine Management: Systems and Components*. Springer Vieweg Wiesbaden, 2014. doi.org/10.1007/978-3-658-03981-3
- [8] Moran, Michael J, Shapiro, Howard N., Boettner, Daisie D., Bailey, Margaret B. *Fundamentals of Engineering Thermodynamics*, 8th Ed. Wiley, 2014.
- [9] Lyn, W.T. "Study of burning rate and nature of combustion in diesel engines," Volume 9, Issue 1, 1963, pp. 1069-1082. [https://doi.org/10.1016/S0082-0784\(63\)80112-5](https://doi.org/10.1016/S0082-0784(63)80112-5)
- [10] Ju, Yiguang. "Understanding cool flames and warm flames," Proceedings of the Combustion Institute, Volume 38, Issue 1, 2021, pp. 83-119. <https://doi.org/10.1016/j.proci.2020.09.019>
- [11] Wang, Yiqing, Chao Xu, Cheng Chi, Zheng Chen, "Direct numerical simulations of turbulent premixed cool flames: Global and local flame dynamics analysis," Combustion and Flame, Volume 270, 2024, <https://doi.org/10.1016/j.combustflame.2024.113759>
- [12] Parker, Allen, Shawn A. Reggeti, Joshua A. Bittle, Ajay K. Agrawal, "Limitations of cetane number to predict transient combustion phenomena in high-pressure fuel sprays," Combustion and Flame, Volume 251, 2023, <https://doi.org/10.1016/j.combustflame.2023.112723>

- [13] Feikema, Douglas A. "Quantitative rainbow schlieren deflectometry as a temperature diagnostic for nonsooting spherical flames." *Appl Opt.* 2006 Jul 10;45(20):4826-32. <https://doi.org/10.1364/ao.45.004826>.
- [14] Parker, A., Agrawal, A. & Bittle, J. "Representative Phenomena of Cyclic Turbulent Combustion in High-Pressure Fuel Sprays." *Flow Turbulence Combust* 111, 675–696 (2023). <https://doi.org/10.1007/s10494-023-00432-3>
- [15] Howes, Walton L., "Rainbow schlieren and its applications," *Appl. Opt.* **23**, 2449-2460, 1984. <https://doi.org/10.1364/AO.23.002449>
- [16] Greenberg, Paul S., Robert B. Klimek, and Donald R. Buchele, "Quantitative rainbow schlieren deflectometry," *Appl. Opt.* 34, 3810-3825, 1995. <https://doi.org/10.1364/AO.34.003810>
- [17] Wanstall, C.T., Bittle, J.A. & Agrawal, A.K. "Quantitative concentration measurements in a turbulent helium jet using rainbow schlieren deflectometry." *Exp Fluids* 62, 53, 2021. <https://doi.org/10.1007/s00348-021-03154-2>
- [18] Wanstall, C. Taber & Agrawal, Ajay & Bittle, Joshua. "Phase boundary detection in transient, evaporating high-pressure fuel sprays by rainbow schlieren deflectometry." *Applied Optics*. 58, 2019. pp. 6791-6801. <https://doi.org/10.1364/AO.58.006791>
- [19] Agrawal, A., Alammar, K. & Gollahalli, S. "Application of rainbow schlieren deflectometry to measure temperature and oxygen concentration in a laminar gas-jet diffusion flame." *Exp Fluids* 32, 689–691 (2002). <https://doi.org/10.1007/s00348-002-0422-y>
- [20] Krisman, Alex, Evatt R. Hawkes, Mohsen Talei, Ankit Bhagatwala, Jacqueline H. Chen. "A direct numerical simulation of cool-flame affected autoignition in diesel engine-relevant conditions," *Proceedings of the Combustion Institute*, Volume 36, Issue 3, 2017, pp. 3567-3575. <https://doi.org/10.1016/j.proci.2016.08.043>
- [21] Musculus, Mark P.B., Paul C. Miles, Lyle M. Pickett, "Conceptual models for partially premixed low-temperature diesel combustion," *Progress in Energy and Combustion Science*, Volume 39, Issues 2–3, 2013, pp. 246-283. <https://doi.org/10.1016/j.pecs.2012.09.001>
- [22] Novoselov, Alex G, Christopher B. Reuter, Omar R. Yehia, Sang Hee Won, Matthew K. Fu, Katherine Kokmanian, Marcus Hultmark, Yiguang Ju, Michael E. Mueller. "Turbulent nonpremixed cool flames: Experimental measurements, Direct Numerical Simulation, and

- manifold-based combustion modeling," Combustion and Flame, Volume 209, 2019, pp. 144-154. <https://doi.org/10.1016/j.combustflame.2019.07.034>
- [23] Waqas, Muhammad, Song Cheng, S. Scott Goldsborough, Toby Rockstroh, Bengt Johansson, Christopher P. Kolodziej. "An experimental and numerical investigation to characterize the low-temperature heat release in stoichiometric and lean combustion," Proceedings of the Combustion Institute, Volume 38, Issue 4, 2021, pp. 5673-5683, <https://doi.org/10.1016/j.proci.2020.07.146>
- [24] Wanstall, C. Taber, Agrawal AK, Bittle JA. "Quantifying liquid boundary and vapor distributions in a fuel spray by rainbow schlieren deflectometry." Appl Opt. 2017 Oct 20;56(30):8385-8393. <https://doi.org/10.1364/AO.56.008385>
- [25] Parker, Allen, C. Taber Wanstall, Shawn A. Reggeti, Joshua A. Bittle, Ajay K. Agrawal. "Simultaneous rainbow schlieren deflectometry and OH\* chemiluminescence imaging of a diesel spray flame in constant pressure flow rig," Proceedings of the Combustion Institute, Volume 38, Issue 4, 2021, pp. 5557-5565. <https://doi.org/10.1016/j.proci.2020.05.045>
- [26] Reggeti, S. A., Parker, A., Wanstall, C. T., Agrawal, A. K., and Bittle, J. A. "Comparing Global Spray Combustion Characteristics and Local Shot-to-Shot Variations in a Reacting n-Heptane Spray." ASME. J. Eng. Gas Turbines Power. September 2021; 143(9): 091018. <https://doi.org/10.1115/1.4050868>
- [27] Li, Shiyang, Yijie Wei, Ning Wang, Shuai Huang, Xinyi Zhou, Jiale Cao, Run Chen, Tie Li. "Dynamic characteristics of pilot injection: Spray evaporation, mixture formation, and combustion under engine-like conditions," Experimental Thermal and Fluid Science, Volume 169, 2025, 111564, <https://doi.org/10.1016/j.expthermflusci.2025.111564>
- [28] Hœpffner, Jérôme & Bewley, Thomas. (2005). "State estimation in wall-bounded flow systems. Part 1. Perturbed laminar flows." Journal of Fluid Mechanics. 534. 263 - 294. <https://doi.org/10.1017/S0022112005004210>
- [29] Frohberg, Fabio, Pablo Kandel, Abdulla Ghani. "Physics-informed neural networks for reacting flows: Species reconstruction with finite rate chemistry from sparse and noisy velocity measurements," Proceedings of the Combustion Institute, Volume 41, 2025, 105957, <https://doi.org/10.1016/j.proci.2025.105957>
- [30] Gonzales, Rafael C., Richard E. Woods. *Digital Image Processing* 4th ed. Pearson Education Limited, 2018.

- [31] Román, Manuel García, Mercedes Márquez Hernández, Pascual Jara, Alain Verschoren. “Uniform filters,” Cahiers de topologie et géométrie différentielle catégoriques, Vol. 40, no 2, 1999, pp. 82-126.
- [32] Marr, D., E. Hildreth. “Theory of edge detection.” Proc Biol Sci 1 February 1980; 207 (1167): 187–217. <https://doi.org/10.1098/rspb.1980.0020>
- [33] Crowley, JL., Parker, AC. “A representation for shape based on peaks and ridges in the difference of low-pass transform.” IEEE Trans Pattern Anal Mach Intell. 1984 Feb;6(2):156-70. <https://doi.org/10.1109/tpami.1984.4767500>
- [34] Haddad, R. A., & A. N. Akansu, "A class of fast Gaussian binomial filters for speech and image processing," in IEEE Transactions on Signal Processing, vol. 39, no. 3, pp. 723-727, March 1991, <https://doi.org/10.1109/78.80892>
- [35] Bloch, Isabelle, Henk Heijmans, Christian Ronse. “Mathematical Morphology,” 2007, pp. 345-359. In Aiello, Marco, Ian Pratt-Hartmann, Johan Benthem. *Handbook of Spatial Logics*. Springer Dordrecht, 2007.
- [36] Serra, Jean Paul Frédéric. “Image Analysis and Mathematical Morphology.” 1983.
- [37] Bishop, Christopher M. *Pattern Recognition and Machine Learning*. Springer Science+Business Media, LLC, 2006.

## **APPENDIX A**

The code used for image analysis can be found at:

<https://github.com/UnivOfAlabama-BittleResearchGroup/SprayChamberREU2025>